Phase-field modelling of fracture in single crystal plasticity

April 11, 2016

Abstract

We propose a phase-field model for ductile fracture in a single crystal within the kinematically linear regime, by combining the theory of single crystal plasticity as formulated in Gurtin et al. (2010) and the phase-field formulation for ductile fracture proposed by Ambati et al. (2015) . The model introduces coupling between plasticity and fracture through the dependency of the so-called degradation function from a scalar global measure of the accumulated plastic strain on all slip systems. A viscous regularization is introduced both in the treatment of plasticity and in the phase-field evolution equation. Testing of the model on two examples for face centred cubic single crystals indicates that fracture is predicted to initiate and develop in the regions of the maximum accumulated plastic strain, which is in agreement with phenomenological observations. A rotation of the crystallographic unit cell is shown to affect the test results in terms of failure pattern and corresponding global and local response.

Keywords: Fracture, Phase-field modeling, Single-crystal plasticity.

1 Introduction

Metals are typically encountered in the form of polycrystalline aggregates, composed of grains separated by grain boundaries, where the structure of the grain interiors is similar to that of a single crystal (see e.g. Gurtin et al., 2010). The distinct feature of crystals is the orientation dependence of the activation of the crystallographic deformation mechanisms (including e.g. dislocations, twins, and martensitic transformations), which induces mechanical anisotropy. In other words, the main mechanical phenomena and properties such as shape change, strain hardening, damage and strength are also orientation dependent (Roters et al., 2010).

The appropriate modelling framework to describe metal single crystals is single-crystal plasticity, which encompasses a large class of models accounting for mechanical anisotropy. As outlined in Gurtin et al. (2010), the foundations of single-crystal plasticity can be traced back to Taylor (1938); Mandel (1965); Hill (1965); Rice (1971); Teodosiu and Sidoroff (1976); Asaro and Needleman (1985); Kalidindi et al. (1992) (see Gurtin et al., 2010, for a more comprehensive review). The theory of single-crystal plasticity has been recast by Gurtin et al. (2010) to one based on the principle of virtual power. Single-crystal plasticity can be used to predict the mechanical behavior of single-crystal specimens under complex loading conditions, but also single-crystal components like turbine blades in jet engines (Cailletaud et al., 2003). The same theory can be used also to derive the behaviour of metal polycrystals from the behaviour of individual grains, by combining the description of sets of interacting grains with a model of the transgranular behaviour (Mika and Dawson, 1998; Staroselsky and Anand, 1998; Barbe et al., 2001; Cailletaud et al., 2003; Gottschalk et al., 2016). Moreover, at low temperatures the macroscopic inelastic response of most polycrystalline metallic materials with grain sizes larger than about 100 nm is primarily due to the inelastic response of the interiors of the single crystals, as the boundaries of the crystals may be assumed to be perfectly bonded (Gurtin et al., 2010).

The focus of this paper is on damage and fracture phenomena. Fracture in metals, and more generally in ductile materials, is known to result from material deterioration occurring upon significant plastic deformation. Fracture prediction has gained increasing interest in the engineering community over the past decades (Besson, 2010). The challenge for computational modelling is to accurately reproduce various behavioural features, including the stress state, ductility, damage patterns, failure mode and corresponding load-carrying

capacity. A comprehensive review of the available modelling approaches has been reported in Besson (2010) and summarized in Ambati et al. (2015).

Among the possible approaches to fracture, the ones which have thus far been applied to single crystals or polycrystals fall within the category of damage models. An anisotropic damage model coupled to crystal viscoplasticity was proposed in Ekh et al. (2004). The authors associated damage to each individual slip system based on experimental results for duplex stainless steel, where the initiation and the propagation of microcracks were found to follow the orientation of the slip planes. Dunne et al. (2007) simulated by means of an isotropic damage model within the crystal plasticity framework their own low cycle fatigue experiments on a polycrystalline nickel-based alloy. They found a strong dependence of the crack nucleation and growth on the microstructural features. In Aslan et al. (2011), a micromorphic approach was developed for the modelling of gradient plasticity and damage in single crystals. The total damage consists of a cleavage and two shear components in the slip plane corresponding to mode I, II and III crack growth. The model was applied to simulate the strain localization to a single slip plane and crack propagation under mode I conditions.

Phase-field fracture models share many features with gradient-enhanced damage models, and have recently emerged as a very promising alternative to discrete formulations due to their ability to deliver crack-like localized damage patterns (Francfort and Marigo, 1998; Bourdin et al., 2000; Amor et al., 2009; Kuhn and Müller, 2010; Miehe et al., 2010; Borden et al., 2012), see also the review paper by Ambati et al. (2014) and the references therein. In these approaches the so-called order parameter (or crack phase field) describes the smooth transition between the intact and fully broken material phases, thus approximating the sharp crack discontinuity. Its evolution models the fracture process dealing naturally with crack nucleation, propagation, merging, and branching without the need for additional ad-hoc criteria, in general situations and for 3D geometries on a fixed mesh. A few very recent contributions deal with phase-field modelling of fracture in ductile materials (see e.g. Ulmer et al., 2013; Borden, 2012; Duda et al., 2015; Ambati et al., 2015; Alessi et al., 2015; Wick et al., 2015). Most relevant for the present investigation is the phase-field model for quasi-static ductile fracture proposed by Ambati et al. (2015) for classical J_2-plasticity in a kinematically linear framework and later extended by Ambati et al. (2016) to large deformations and by Ambati and De Lorenzis (2016) to modelling of fracture in shells. A thermodynamically consistent coupling between plasticity and fracture was introduced here by letting the so-called stress degradation function depend on a scalar cumulative measure of the plastic strain, which leads to a strong influence of the accumulated plastic strains on the evolution of the phase field. This feature of the model was shown to allow for the correct prediction of some important phenomenological features of ductile fracture. A preliminary investigation on phase-field modelling applied to fracture in single-crystal plasticity has been reported by Hernandez Padilla and Markert (2015), where the fracture problem of a squared plate under tension in plane stress conditions has been examined.

The focus of this work is on modelling and simulation of ductile damage and fracture in a single crystal within the kinematically linear regime. The basic idea is to combine the theory of single crystal plasticity as formulated in Gurtin et al. (2010) and the phase-field formulation for ductile fracture proposed in Ambati et al. (2015). The developed modelling approach can be used to simulate the failure behaviour of single crystals and can be later extended to the case of polycrystals.

The paper is structured as follows: the governing equations of the proposed quasi-static ductile fracture model within the single-crystal plasticity framework are outlined in Section 2, whereas Section 3 formulates the incremental variational problem and its numerical solution in the discretized setting with the finite element method. In Section 4, we present and discuss several numerical examples. Conclusions are drawn in

Section 5.

2 Governing equations

2.1 Kinematics

Consider a continuum body occupying the domain B shown in Fig. 1. A typical material point is identified by the position vector $\boldsymbol{x}$. The displacement of the material point with time t is denoted by $\boldsymbol{u}(\boldsymbol{x}, t)$. Infinitesimal deformations are assumed. The displacement gradient $\boldsymbol{H} := \nabla \boldsymbol{u}$ is decomposed (locally) into elastic and plastic parts, denoted $\boldsymbol{H}^{\mathrm{e}}$ and $\boldsymbol{H}^{\mathrm{p}}$ respectively, according to

$$\boldsymbol{H} = \nabla \mathbf{u} = \mathbf{H}^{\mathrm{e}} + \mathbf{H}^{\mathrm{p}} \,. \tag{1}$$ eq:Gradu

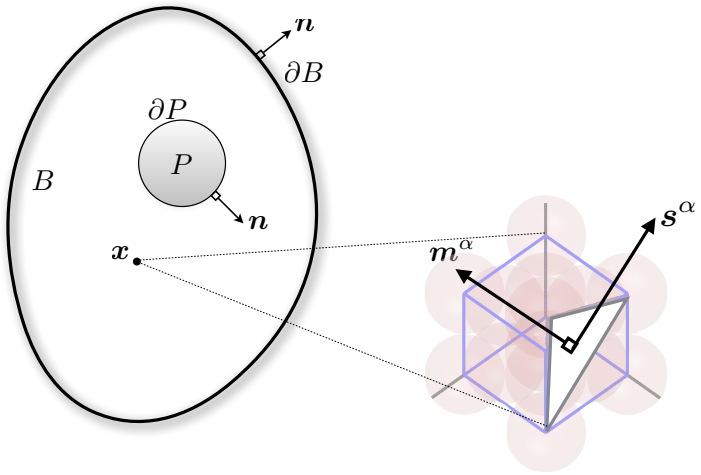

Figure 1: The continuum body B with boundary ∂B. The location of a material point $\boldsymbol{x}$ is indicated as well as a depiction of the kinematic model of plastic slip on a slip system within a unit cell. An arbitrary control region P is also shown.
⟨kinematics⟩

The fundamental kinematic assumption of crystal plasticity is the existence of A slip systems, each characterized by a plane with unit normal $\mathbf{m}^\alpha$ and by a slip direction $\mathbf{s}^\alpha$ on that plane ($\mathbf{s}^\alpha \cdot \mathbf{m}^\alpha = 0$ and $|\mathbf{s}^\alpha| = |\mathbf{m}^\alpha| = 1$), with the corresponding plastic slip denoted as γ^α, $\alpha = 1, ..., A$. The slip system associated with $\boldsymbol{s}^\alpha$ and $\boldsymbol{m}^\alpha$ is denoted by Γ^α. The flow of dislocations through the crystal lattice is described kinematically via the assumption that the plastic distortion tensor $\boldsymbol{H}^{\mathrm{p}}$ is given by

$$\boldsymbol{H}^{\mathrm{p}} = \sum_\alpha \gamma^\alpha \underbrace{(\boldsymbol{s}^\alpha \otimes \boldsymbol{m}^\alpha)}_{\boldsymbol{S}^\alpha} , \tag{2}$$ eq:Hp

where $\boldsymbol{S}^\alpha$ is the Schmidt tensor. The total strain $\boldsymbol{E}$ is given by

$$\boldsymbol{E} = \frac{1}{2}\left(\boldsymbol{H} + \boldsymbol{H}^{\mathsf{T}}\right) ,$$

and is assumed decomposable into elastic and plastic parts so that

$$\boldsymbol{E} = \boldsymbol{E}^{\mathrm{e}} + \boldsymbol{E}^{\mathrm{p}} \,.$$

In particular, from eqs. (1)–(2) the plastic component of the strain is defined by

$$\mathbf{E}^{\mathrm{p}} = \frac{1}{2} \sum_{\alpha} \gamma^{\alpha} \left(\boldsymbol{S}^{\alpha} + \boldsymbol{S}^{\alpha \mathsf{T}} \right) = \sum_{\alpha} \gamma^{\alpha} \boldsymbol{S}^{\alpha}_{\mathrm{sym}} \,,$$

where $\boldsymbol{S}^{\alpha}_{\mathrm{sym}}$ is the symmetric Schmidt tensor for Γ^{α}. Any array associated with the set of A slip systems is denoted $\underline{\gamma} := \{\gamma^1 \,, \gamma^2 \,\ldots\,, \gamma^A\}$. Summation over the slip systems will be abbreviated by $\sum_{\alpha}$. The summation convention is *not* employed in respect of indices relating to the slip systems.

2.2 Balance equations

alance-equations⟩

The form of the governing relations is determined from a virtual power balance (see e.g. Gurtin et al., 2010, for further details).

The internal power $\mathcal{I}$ over a subregion $P \subset B$ is assumed to take the form

$$\mathcal{I}\,(P) = \int\limits_{P} \boldsymbol{T} : \dot{\boldsymbol{H}}^{\mathrm{e}} \, dv + \sum_{\alpha} \int\limits_{P} \pi^{\alpha} \dot{\gamma}^{\alpha} \, dv + \int\limits_{P} \boldsymbol{\xi} \cdot \nabla \dot{s} \, dv + \int\limits_{P} \pi \dot{s} \, dv \,, \tag{3}$$

internal_power

where $\boldsymbol{T}$ is the Cauchy stress (power conjugate to $\dot{\boldsymbol{H}}^{\mathrm{e}}$), π^{α} is the microscopic force associated with Γ^{α} (power-conjugate to the slip rate $\dot{\gamma}^{\alpha}$), $\boldsymbol{\xi}$ is the microscopic stress (power conjugate to $\nabla \dot{s}$), and π is the microscopic internal body force (power-conjugate to $\dot{s}$). The field variable s indicates the degree of intactness of the material (the so-called *crack field parameter* or simply the *phase field*) and varies smoothly from 1 (undamaged material) to 0 (totally broken).

The external power $\mathcal{W}$ acting on $P \subset B$ is given by

$$\mathcal{W}\,(P) = \int\limits_{\partial P} \boldsymbol{t}\,(\boldsymbol{n}) \cdot \dot{\boldsymbol{u}} \, da + \int\limits_{P} \boldsymbol{b} \cdot \dot{\boldsymbol{u}} \, dv + \int\limits_{\partial P} \chi\,(\boldsymbol{n})\, \dot{s} \, da + \int\limits_{P} \gamma \dot{s} \, dv \,,$$

where $\boldsymbol{t}$ is the traction vector on the elementary area da of the surface ∂P, with outward unit normal $\boldsymbol{n}$, $\boldsymbol{b}$ is the macroscopic body force, χ and γ are respectively the microscopic external traction and the microscopic external body force, both power-conjugate to $\dot{s}$.

Consider a generalized virtual velocity $\mathcal{V}$ defined by

$$\mathcal{V} = \left(\widetilde{\boldsymbol{u}}, \widetilde{\boldsymbol{H}}^{\mathrm{e}}, \underline{\widetilde{\gamma}}, \widetilde{s} \right) \,,$$

satisfying the following kinematic constraints arising from eqs. (1)–(2):

$$\nabla \widetilde{\boldsymbol{u}} = \widetilde{\boldsymbol{H}}^{\mathrm{e}} + \sum_{\alpha} \widetilde{\gamma}^{\alpha} \boldsymbol{S}^{\alpha} \,.$$

The principle of virtual power $\mathcal{I}(P) = \mathcal{W}(P)$ reads

$$\int_P \boldsymbol{T} : \widetilde{\boldsymbol{H}}^{\mathrm{e}}\, dv + \sum_\alpha \int_P \pi^\alpha \widetilde{\gamma}^\alpha\, dv + \int_P \boldsymbol{\xi}\cdot\nabla\widetilde{s}\, dv + \int_P \pi\widetilde{s}\, dv = \int_{\partial P} \boldsymbol{t}(\boldsymbol{n})\cdot\widetilde{\boldsymbol{u}}\, da + \int_P \boldsymbol{b}\cdot\widetilde{\boldsymbol{u}}\, dv + \int_{\partial P} \chi(\boldsymbol{n})\,\widetilde{s}\, da + \int_P \gamma\widetilde{s}\, dv \quad (4)$$ eq:PVP

for any subregion P of the body B, and for all $\mathcal{V}$. Various choices of the generalized virtual velocity $\mathcal{V}$ are now made in order to obtain the governing relations.

The choice of $\mathcal{V} \equiv (\widetilde{\boldsymbol{u}}, \nabla\widetilde{\boldsymbol{u}}, \underline{0}, 0)$ in eq. (4) leads to the *macroscopic force balance*

$$\mathrm{div}\boldsymbol{T} + \boldsymbol{b} = \boldsymbol{0} \quad (5)$$ eq:mom_bal

and to the expression for the *macroscopic traction*

$$\boldsymbol{t}(\boldsymbol{n}) = \boldsymbol{T}\boldsymbol{n}\,. \quad (6)$$ {?}

The symmetry of the stress tensor $\boldsymbol{T}$ follows from choosing a virtual elastic rigid body motion $\widetilde{\boldsymbol{u}} \equiv \widetilde{\boldsymbol{a}} + \boldsymbol{\lambda}\times\boldsymbol{x} = \widetilde{\boldsymbol{a}} + \boldsymbol{\Lambda}\boldsymbol{x}$, where $\boldsymbol{\lambda}$ is the axial vector and $\boldsymbol{\Lambda}$ the associated skew-tensor where $\boldsymbol{\Lambda} = -\boldsymbol{\Lambda}^{\mathsf{T}}$. Thus with $\mathcal{V} = (\widetilde{\boldsymbol{u}}, \nabla\widetilde{\boldsymbol{u}}, \underline{0}, 0)$, the symmetry of $\boldsymbol{T}$ follows from eq. (4) (see e.g. Gurtin et al., 2010, for further details).

Choosing a virtual velocity of the form $\mathcal{V} \equiv \left(\boldsymbol{0}, -\sum_\alpha \widetilde{\gamma}^\alpha \boldsymbol{S}^\alpha, \underline{\widetilde{\gamma}}, 0\right)$ yields the *plastic microscopic force balance*:

$$\tau^\alpha = \pi^\alpha\,, \quad (7)$$ eq:microbalance

where

$$\tau^\alpha = \boldsymbol{S}^\alpha : \boldsymbol{T} = \boldsymbol{s}^{\boldsymbol{\alpha}}\cdot\boldsymbol{T}\boldsymbol{m}^{\boldsymbol{\alpha}}$$

is the Schmidt stress (i.e. the projection of the stress tensor $\boldsymbol{T}$ on Γ^α).

Finally, insertion in eq. (4) of a virtual velocity $\mathcal{V} \equiv (\boldsymbol{0}, \boldsymbol{0}, \underline{0}, \widetilde{s})$ yields

$$\int_P \boldsymbol{\xi}\cdot\nabla\widetilde{s}\, dv + \int_P \pi\widetilde{s}\, dv = \int_{\partial P} \chi(\boldsymbol{n})\,\widetilde{s}\, da + \int_P \gamma\widetilde{s}\, dv\,. \quad (8)$$ eq:PVP-1

Through the divergence theorem, eq. (8) leads to the *phase-field microscopic force balance*

$$\mathrm{div}\boldsymbol{\xi} - \pi + \gamma = 0\,, \quad (9)$$ eq:microbal

and to the expression for the *phase-field microscopic traction*

$$\chi(\boldsymbol{n}) = \boldsymbol{\xi}\cdot\boldsymbol{n}\,.$$

2.3 Dissipation inequality and constitutive laws

Following the formulation in Section 2.2, the dissipation inequality can be written (in local form) as

$$\dot{\psi} - \boldsymbol{T} : \dot{\boldsymbol{E}}^{\mathrm{e}} - \sum_\alpha \pi^\alpha\dot{\gamma}^\alpha - \boldsymbol{\xi}\cdot\nabla\dot{s} - \pi\dot{s} = -D \le 0\,, \quad (10)$$ eq:diss_ineq-1

where ψ is the free energy and $D \geq 0$ is the dissipation rate, both per unit volume. The second to final terms on the left hand side of eq. (10) represent the local form of the internal power defined in eq. (3).

Consider, most generally, a free energy of the form given by

$$\psi = \hat{\psi}\left(\boldsymbol{E}^{\mathrm{e}}, e^{\mathrm{p}}, \underline{\eta}, s, \nabla s, \dot{s}\right) . \tag{11}$$ eq:psi

This postulated form contains the "standard" dependencies on the elastic strain $\boldsymbol{E}^{\mathrm{e}}$ and on a set of hardening variables $\underline{\eta}$. In addition, further dependencies on the phase field, on its gradient and on its rate, as well as on e^{p} are included. The latter is a *local scalar* measure of plastic strain accumulation defined by

$$\dot{e}^{\mathrm{p}} = \sum_{\alpha} |\dot{\gamma}^{\alpha}| \geq 0 \qquad \text{where} \qquad e^{\mathrm{p}}(t) = \sum_{\alpha} \int_{0}^{t} |\dot{\gamma}^{\alpha}| \, d\tau \, . \tag{12}$$ eq:e_p

The dependence of the free energy on e^{p} is required to realize the coupling between the evolution of the phase-field parameter s and the accumulation of plastic strain, and is an essential ingredient of the proposed model. Substitution of eq. (11) into the dissipation inequality (10) yields

$$\left(\frac{\partial\hat{\psi}}{\partial\boldsymbol{E}^{\mathrm{e}}} - \boldsymbol{T}\right) : \dot{\boldsymbol{E}}^{\mathrm{e}} + \frac{\partial\hat{\psi}}{\partial e^{\mathrm{p}}}\dot{e}^{\mathrm{p}} - \sum_{\alpha}\pi^{\alpha}\dot{\gamma}^{\alpha} + \sum_{\alpha}\frac{\partial\hat{\psi}}{\partial\eta^{\alpha}}\dot{\eta}^{\alpha} + \left(\frac{\partial\hat{\psi}}{\partial s} - \pi\right)\dot{s} + \left(\frac{\partial\hat{\psi}}{\partial\nabla s} - \boldsymbol{\xi}\right)\cdot\nabla\dot{s} + \frac{\partial\hat{\psi}}{\partial\dot{s}}\ddot{s} = -D \leq 0 \, . \tag{13}$$ eq:diss_ineq

Well-known arguments (see e.g. Gurtin et al., 2010, and the references therein) lead immediately to the *elastic constitutive relationship* for the Cauchy stress given by

$$\boldsymbol{T} = \frac{\partial\hat{\psi}}{\partial\boldsymbol{E}^{\mathrm{e}}} \, . \tag{14}$$ eq:macro_const

Additional consequences of the dissipation inequality can be derived by applying the inequality individually to the group of terms related to the phase field, that is, requiring that

$$\left(\frac{\partial\hat{\psi}}{\partial s} - \pi\right)\dot{s} + \left(\frac{\partial\hat{\psi}}{\partial\nabla s} - \boldsymbol{\xi}\right)\cdot\nabla\dot{s} + \frac{\partial\hat{\psi}}{\partial\dot{s}}\ddot{s} \leq 0 \, . \tag{15}$$ eq:phase

From this restricted inequality follows the *phase-field microscopic constitutive equation* given by

$$\boldsymbol{\xi} = \frac{\partial\hat{\psi}}{\partial\nabla s} \, , \tag{16}$$ eq:micro_const

and the additional equation

$$\frac{\partial\hat{\psi}}{\partial\dot{s}}\ddot{s} = 0 \, . \tag{17}$$ eq:s_dot

Eqs. (16) and (17) indicate that the free energy and thus also the microscopic stress cannot depend on $\dot{s}$ but only depend on s and ∇s. The further reduced inequality (15) thus reads

$$\left(\frac{\partial\hat{\psi}}{\partial s} - \pi\right)\dot{s} \leq 0 \, . \tag{18}$$ eq:phase-1

Assume that the microscopic internal body force π can be decomposed into energetic π_{en} and dissipative

π_{dis} parts as follows

$$\pi = \pi_{\text{en}} + \pi_{\text{dis}} \qquad \text{where} \qquad \pi_{\text{en}} := \frac{\partial \hat{\psi}}{\partial s}\,. \tag{19}$$ eq:pi

The inequality (18) becomes

$$D^s := \pi_{\text{dis}} \dot{s} \geq 0\,, \tag{20}$$?eq:Ds?

which suggests a suitable choice of π_{dis} as

$$\pi_{\text{dis}} = \beta \dot{s} \qquad \text{where} \qquad \beta \geq 0 \tag{21}$$ eq:pi_dis

is a constitutive parameter. Thus the dissipation rate D^s becomes

$$D^s = \beta \dot{s}^2 \geq 0\,.$$

Note that D^s can be considered as the dissipation rate associated with the phase field. From eqs. (19) and (21) it follows

$$\pi = \frac{\partial \hat{\psi}}{\partial s} + \beta \dot{s}\,. \tag{22}$$ eq:pi-1

Substitution of eqs. (16) and (22) into (9) leads to the *phase-field evolution equation* given by

$$\operatorname{div}\left(\frac{\partial \hat{\psi}}{\partial \nabla s}\right) - \frac{\partial \hat{\psi}}{\partial s} - \beta \dot{s} = 0\,, \tag{23}$$ eq:evol_eq

where it has been assumed that the microscopic external body force $\gamma = 0$. Note that the term $\beta \dot{s}$ leads to the rate dependency of eq. (23), the rate-independent case being recovered for $\beta = 0$.

As a result of eq. (14) and inequality (15), from (13) the reduced dissipation inequality becomes

$$\frac{\partial \hat{\psi}}{\partial e^{\text{p}}} \dot{e}^{\text{p}} - \sum_\alpha \pi^\alpha \dot{\gamma}^\alpha + \sum_\alpha \frac{\partial \hat{\psi}}{\partial \eta^\alpha} \dot{\eta}^\alpha \leq 0\,. \tag{24}$$ eq:red_diss_ineq

Introducing the thermodynamic force g^α power-conjugate to $\dot{\eta}^\alpha$ as

$$g^\alpha := -\frac{\partial \hat{\psi}}{\partial \eta^\alpha}\,, \tag{25}$$ eq:g^alfa

and changing sign, eq. (24) takes the final form

$$D^{\text{p}} := \sum_\alpha \pi^\alpha \dot{\gamma}^\alpha + \sum_\alpha g^\alpha \dot{\eta}^\alpha - \frac{\partial \hat{\psi}}{\partial e^{\text{p}}} \dot{e}^{\text{p}} \geq 0\,, \tag{26}$$ eq:red_diss_ineq

where we have denoted by D^{p} the plastic dissipation rate. Since e^{p} is by definition non-negative, inequality (26) can be further reduced to its "classical" version

$$\sum_\alpha (\pi^\alpha \dot{\gamma}^\alpha + g^\alpha \dot{\eta}^\alpha) \geq 0\,, \tag{27}$$ eq:red_diss_ineq

provided that the following inequality holds:

$$\frac{\partial \hat{\psi}}{\partial e^{\mathrm{p}}} \leq 0\,. \tag{28}$$ eq:dpsi_dep

The specific choice of the free energy in the next section will ensure that eq. (28) holds.

2.4 A specific choice of the free energy

Let us now introduce a specific choice of the free energy, as follows

$$\psi = \hat{\psi}^{\mathrm{ec}}(\boldsymbol{E}^{\mathrm{e}}, s, e^{\mathrm{p}}) + \hat{\psi}^{\mathrm{h}}(\underline{\eta}) + \hat{\psi}^{c}(s, \nabla s)\,. \tag{29}$$ eq:psi-1

The elastic contribution $\hat{\psi}^{\mathrm{ec}}$ is given by

$$\hat{\psi}^{\mathrm{ec}}(\boldsymbol{E}^{\mathrm{e}}, s, e^{\mathrm{p}}) = g\left(s, e^{\mathrm{p}}\right) \hat{\psi}^{\mathrm{e}}_{+}(\boldsymbol{E}^{\mathrm{e}}) + \hat{\psi}^{\mathrm{e}}_{-}(\boldsymbol{E}^{\mathrm{e}}) \tag{30}$$ eq:psi_ec

with

$$\hat{\psi}^{\mathrm{e}}_{+}(\boldsymbol{E}^{\mathrm{e}}) = \frac{1}{2}\kappa \left\langle \mathrm{tr}\left(\boldsymbol{E}^{\mathrm{e}}\right)\right\rangle_{+}^{2} + \mu\left(\boldsymbol{E}^{\mathrm{e}}_{\mathrm{dev}} : \boldsymbol{E}^{\mathrm{e}}_{\mathrm{dev}}\right) \qquad \text{and} \qquad \hat{\psi}^{\mathrm{e}}_{-}(\boldsymbol{E}^{\mathrm{e}}) = \frac{1}{2}\kappa \left\langle \mathrm{tr}\left(\boldsymbol{E}^{\mathrm{e}}\right)\right\rangle_{-}^{2}\,, \tag{31}$$ eq:plus_minus

under the assumption of an isotropic elastic response, which will be removed at a later stage, and with the choice of a volumetric / deviatoric split of the elastic strain energy as in Amor et al. (2009). Note that the coupling of the elastic strain field to the phase field and to the plastic strain field is realized through the degradation function $g\left(s, e^{\mathrm{p}}\right)$. In eq. (31), $\kappa = \lambda + \frac{2}{3}\mu$ is the bulk modulus, where λ and μ are the Lamé constants. The notation $\langle a \rangle_{\pm} := \frac{1}{2}\left(a \pm |a|\right)$ denotes the positive and negative parts of an expression a, and $\boldsymbol{E}^{\mathrm{e}}_{\mathrm{dev}} := \boldsymbol{E}^{\mathrm{e}} - \boldsymbol{E}^{\mathrm{e}}_{\mathrm{vol}}$ is the deviatoric component of the elastic strain tensor, the volumetric component being $\boldsymbol{E}^{\mathrm{e}}_{\mathrm{vol}} := \frac{1}{3}\mathrm{tr}\left(\boldsymbol{E}^{\mathrm{e}}\right)\boldsymbol{I}$, with $\boldsymbol{I}$ the second-order unit tensor. From eqs. (29) and (30) it follows that

$$\frac{\partial \hat{\psi}}{\partial e^{\mathrm{p}}} = \frac{\partial g}{\partial e^{\mathrm{p}}} \hat{\psi}^{\mathrm{e}}_{+}(\boldsymbol{E}^{\mathrm{e}})$$

and therefore inequality (28) holds (and the reduced dissipation inequality takes the form given in eq. (27)), provided that

$$\frac{\partial g}{\partial e^{\mathrm{p}}} \leq 0\,. \tag{32}$$ eq:dpsi_dep-1

A possible choice of $g\left(s, e^{\mathrm{p}}\right)$ complying with eq. (32) is

$$g\left(s, e^{\mathrm{p}}\right) = s^{2e^{\mathrm{p}}/e^{\mathrm{p}}_{\mathrm{crit}}} \tag{33}$$ eq:degrad

with $e^{\mathrm{p}}_{\mathrm{crit}} > 0$ a constant threshold value, to be calibrated through comparison with experimental results. Eq. (14) together with (29) and (30) leads to the following decoupled expression for the macroscopic stress $\boldsymbol{T}$

$$\boldsymbol{T} = g\left(s, e^{\mathrm{p}}\right) \frac{\partial \hat{\psi}^{\mathrm{e}}_{+}\left(\boldsymbol{E}^{\mathrm{e}}\right)}{\partial \boldsymbol{E}^{\mathrm{e}}} + \frac{\partial \hat{\psi}^{\mathrm{e}}_{-}\left(\boldsymbol{E}^{\mathrm{e}}\right)}{\partial \boldsymbol{E}^{\mathrm{e}}}\,.$$

For the plastic hardening contribution to the free energy, $\hat{\psi}^{\mathrm{h}}(\underline{\eta})$, the simplest choice is the quadratic

function

$$\hat{\psi}^{\mathrm{h}}(\underline{\eta}) = \frac{1}{2}\sum_{\alpha,\beta} H^{\alpha\beta}\eta^{\alpha}\eta^{\beta} \tag{34}$$ eq:psi-1-1-1

with

$$H^{\alpha\beta} = \begin{cases} H_0 & \beta = \alpha\,, \\ \widetilde{\rho} H_0 & \beta \neq \alpha\,, \end{cases}$$

where H_0 and $\widetilde{\rho}$ are prescribed positive constants, $\widetilde{\rho}$ being chosen in such a way that the matrix with components $H^{\alpha\beta}$ is positive definite. From eq. (25) it follows that

$$g^{\alpha} = -\sum_{\beta} H^{\alpha\beta}\eta^{\beta}$$

Alternative hardening models that distinguish between self- and latent-hardening contributions have been developed by Peirce et al. (1983), among others.

Finally, the phase-field contribution to the free energy is taken as (see Bourdin et al., 2000):

$$\hat{\psi}_c(s, \nabla s) = G_c \left[\frac{1}{4l}(1-s)^2 + l\,|\nabla s|^2 \right].$$

Here G_c is the material fracture toughness and l is a length scale controlling the width of the diffusing region approximating a discrete crack. The microscopic phase-field constitutive equation (16) yields

$$\boldsymbol{\xi} = \frac{\partial \hat{\psi}}{\partial \nabla s} = 2G_c l \nabla s\,, \tag{35}$$ eq:csi

and the phase-field evolution equation (23) becomes

$$2l\nabla^2 s + \frac{1-s}{2l} = \frac{1}{G_c}\frac{\partial g}{\partial s}\hat{\psi}^{\mathrm{e}}_{+}(\boldsymbol{E}^{\mathrm{e}}) + \frac{\beta}{G_c}\dot{s}\,. \tag{36}$$ eq:evol_eq_gen

For the specific choice of $g(s, e^{\mathrm{p}})$ in eq. (33) the phase field evolution equation becomes

$$2l\nabla^2 s + \frac{1-s}{2l} = \frac{2p}{G_c}\hat{\psi}^{\mathrm{e}}_{+}(\boldsymbol{E}^{\mathrm{e}})\, s^{2p-1} + \frac{\beta}{G_c}\dot{s} \tag{37}$$ eq:evol_eq_1

with $p := e^{\mathrm{p}}/e^{\mathrm{p}}_{\mathrm{crit}}$.

2.5 Effect of elastic anisotropy

The split of the volumetric and deviatoric parts of the elastic energy presented in eq. (31) assumed an isotropic elastic response. This assumption is not appropriate for a range of crystalline materials. The split of the elastic energy is now extended to account for cubic symmetry as found in face-centred cubic (FCC) crystalline materials, for example.

The slip directions and slip plane normals for the slip systems of a FCC crystal relative to the crystal unit cell, denoted respectively as $\overline{\boldsymbol{s}}^{\alpha}$ and $\overline{\boldsymbol{m}}^{\alpha}$, are listed in Table 1. These are related to the corresponding vectors in the fixed orthonormal reference frame via $\overline{\boldsymbol{s}}^{\alpha} = \boldsymbol{R}\boldsymbol{s}^{\alpha}$ and $\overline{\boldsymbol{m}}^{\alpha} = \boldsymbol{R}\boldsymbol{m}^{\alpha}$, where $\boldsymbol{R} := \boldsymbol{\Theta}_3\boldsymbol{\Theta}_2\boldsymbol{\Theta}_1$ is

the rotation matrix, with

$$\boldsymbol{\Theta}_1 = \begin{bmatrix} \cos\vartheta_1 & \sin\vartheta_1 & 0 \\ -\sin\vartheta_1 & \cos\vartheta_1 & 0 \\ 0 & 0 & 1 \end{bmatrix}, \qquad \boldsymbol{\Theta}_2 = \begin{bmatrix} \cos\vartheta_2 & 0 & -\sin\vartheta_2 \\ 0 & 1 & 0 \\ \sin\vartheta_2 & 0 & \cos\vartheta_2 \end{bmatrix}, \qquad \boldsymbol{\Theta}_3 = \begin{bmatrix} \cos\vartheta_3 & \sin\vartheta_3 & 0 \\ -\sin\vartheta_3 & \cos\vartheta_3 & 0 \\ 0 & 0 & 1 \end{bmatrix},$$

and with Euler angles $\{\vartheta_1, \vartheta_2, \vartheta_3\}$.

Assuming cubic symmetry for the elastic response, the components of the fourth-order elasticity tensor $\overline{\mathcal{C}}$ in the reference system of the crystal unit cell are given by

$$\overline{\mathcal{C}}_{ijkl} = C_{12}\delta_{ij}\delta_{kl} + C_{44}\left(\delta_{ik}\delta_{jl} + \delta_{il}\delta_{jk}\right) + \overline{C}\sum_{R=1}^{3}\delta_{ir}\delta_{jr}\delta_{kr}\delta_{lr}\,, \tag{38}$$ eq:C_bar

where $\overline{C} = C_{11} - C_{12} - 2C_{44}$, (see e.g. Dederichs and Leibfried, 1969). For the special case of elastic isotropy we have

$$C_{11} = \kappa + \tfrac{4}{3}\mu\,, \qquad C_{12} = \kappa - \tfrac{2}{3}\mu\,, \qquad C_{44} = \mu\,,$$

resulting in $\overline{C} \equiv 0$. Denoting by $\overline{\boldsymbol{E}}^{\mathrm{e}} := \boldsymbol{R}\boldsymbol{E}^{\mathrm{e}}\boldsymbol{R}^{\mathsf{T}}$ the elastic strain tensor in the reference system of the crystal unit cell, the (undamaged) elastic free energy (see eq. (30)) can be expressed as

$$\begin{aligned}\hat{\psi}^{\mathrm{ec}}\left(\bar{\boldsymbol{E}}^{\mathrm{e}}\right) &= \frac{1}{2}\bar{\boldsymbol{E}}^{\mathrm{e}} : \overline{\mathcal{C}}\,\bar{\boldsymbol{E}}^{\mathrm{e}} \\ &= \frac{1}{2}C_{12}(\bar{E}^{\mathrm{e}}_{ii})^2 + C_{44}\bar{E}^{\mathrm{e}}_{jk}\bar{E}^{\mathrm{e}}_{jk} + \frac{\overline{C}}{2}\sum_{r=1}^{3}(\bar{E}^{\mathrm{e}}_{rr})^2\,.\end{aligned}$$

In order to generalize the decomposition of the elastic free energy in eq. (31) to the anisotropic case, we note that the volumetric/deviatoric split of the elastic strain tensor leads to an analogous split of the elastic free energy, that is,

$$\hat{\psi}^{\mathrm{ec}}\left(\bar{\boldsymbol{E}}^{\mathrm{e}}\right) = \hat{\psi}^{\mathrm{e}}_{\mathrm{vol}}\left(\bar{\boldsymbol{E}}^{\mathrm{e}}_{\mathrm{vol}}\right) + \hat{\psi}^{\mathrm{e}}_{\mathrm{dev}}\left(\bar{\boldsymbol{E}}^{\mathrm{e}}_{\mathrm{dev}}\right)$$

with

$$\begin{aligned}\hat{\psi}^{\mathrm{e}}_{\mathrm{vol}}\left(\bar{\boldsymbol{E}}^{\mathrm{e}}_{\mathrm{vol}}\right) &= \frac{1}{2}\bar{\boldsymbol{E}}^{\mathrm{e}}_{\mathrm{vol}} : \overline{\mathcal{C}}\,\bar{\boldsymbol{E}}^{\mathrm{e}}_{\mathrm{vol}} \\ \hat{\psi}^{\mathrm{e}}_{\mathrm{dev}}\left(\bar{\boldsymbol{E}}^{\mathrm{e}}_{\mathrm{dev}}\right) &= \frac{1}{2}\bar{\boldsymbol{E}}^{\mathrm{e}}_{\mathrm{dev}} : \overline{\mathcal{C}}\,\bar{\boldsymbol{E}}^{\mathrm{e}}_{\mathrm{dev}}\,.\end{aligned} \tag{39}$$ eq:vol

The combination of eq. (39) and eq. (38) allows one to express the volumetric part of the elastic free energy

as follows

$$\begin{aligned}\hat{\psi}^{\mathrm{e}}_{\mathrm{vol}}\left(\bar{\boldsymbol{E}}^{\mathrm{e}}_{\mathrm{vol}}\right) &= \frac{1}{2}\bar{E}^{\mathrm{e}}_{\mathrm{vol}\,ij}\overline{\mathcal{C}}_{ijkl}\bar{E}^{\mathrm{e}}_{\mathrm{vol}\,kl}\\ &= \frac{1}{2}\frac{1}{3}\bar{E}^{\mathrm{e}}_{mm}\delta_{ij}\left[C_{12}\delta_{ij}\delta_{kl}+C_{44}\left(\delta_{ik}\delta_{jl}+\delta_{il}\delta_{jk}\right)+\overline{C}\delta_{ir}\delta_{jr}\delta_{kr}\delta_{lr}\right]\frac{1}{3}\bar{E}^{\mathrm{e}}_{nn}\delta_{kl}\\ &= \frac{1}{2}\underbrace{\left[C_{12}+\frac{2}{3}C_{44}+\frac{1}{3}\overline{C}\right]}_{\overline{\kappa}}(\mathrm{tr}\bar{\boldsymbol{E}}^{\mathrm{e}})^2\,.\end{aligned}$$

In the special case of isotropy, $\overline{\kappa}\equiv\kappa=\lambda+2/3\mu$ (i.e. the bulk modulus) and the standard result is recovered. The deviatoric component yields

$$\begin{aligned}\hat{\psi}^{\mathrm{e}}_{\mathrm{dev}}\left(\bar{\boldsymbol{E}}^{\mathrm{e}}_{\mathrm{dev}}\right) &= \frac{1}{2}\bar{E}^{\mathrm{e}}_{\mathrm{dev}\,ij}\overline{\mathcal{C}}_{ijkl}\bar{E}^{\mathrm{e}}_{\mathrm{dev}\,kl}\\ &= \frac{1}{2}\bar{E}^{\mathrm{e}}_{\mathrm{dev}\,ij}\left[C_{12}\delta_{ij}\delta_{kl}+C_{44}\left(\delta_{ik}\delta_{jl}+\delta_{il}\delta_{jk}\right)+\overline{C}\delta_{ir}\delta_{jr}\delta_{kr}\delta_{lr}\right]\bar{E}^{\mathrm{e}}_{\mathrm{dev}\,kl}\\ &= C_{44}\bar{\boldsymbol{E}}^{\mathrm{e}}_{\mathrm{dev}}:\bar{\boldsymbol{E}}^{\mathrm{e}}_{\mathrm{dev}}+\frac{1}{2}\overline{C}\sum_{r=1}^{3}(\bar{E}^{\mathrm{e}}_{\mathrm{dev}\,rr})^2\,.\end{aligned}$$

Based on the above derivations, the elastic strain energy adopted in the present work for the anisotropic case is still given by (30) with

$$\hat{\psi}^{\mathrm{e}}_{+}(\boldsymbol{E}^{\mathrm{e}})=\frac{1}{2}\overline{\kappa}\left\langle\mathrm{tr}\left(\boldsymbol{E}^{\mathrm{e}}\right)\right\rangle^2_{+}+C_{44}\left(\boldsymbol{E}^{\mathrm{e}}_{\mathrm{dev}}:\boldsymbol{E}^{\mathrm{e}}_{\mathrm{dev}}\right)+\frac{1}{2}\overline{C}\sum_{r=1}^{3}(\bar{E}^{\mathrm{e}}_{\mathrm{dev}\,rr})^2\quad\text{and}\quad\hat{\psi}^{\mathrm{e}}_{-}(\boldsymbol{E}^{\mathrm{e}})=\frac{1}{2}\overline{\kappa}\left\langle\mathrm{tr}\left(\boldsymbol{E}^{\mathrm{e}}\right)\right\rangle^2_{-}\,.$$

Table 1: The orientations of the slip systems for a FCC crystal relative to the unit cell. The vectors $\overline{\boldsymbol{s}}^{\alpha}$ and $\overline{\boldsymbol{m}}^{\alpha}$ denote respectively the slip direction and the slip plane normal relative to the crystal lattice.

α	$\overline{\boldsymbol{s}}^{\alpha}$	$\overline{\boldsymbol{m}}^{\alpha}$	α	$\overline{\boldsymbol{s}}^{\alpha}$	$\overline{\boldsymbol{m}}^{\alpha}$	α	$\overline{\boldsymbol{s}}^{\alpha}$	$\overline{\boldsymbol{m}}^{\alpha}$
1	$[\overline{1}\ 1\ 0]$	$(1\ 1\ 1)$	5	$[1\ 0\ 1]$	$(1\ \overline{1}\ \overline{1})$	9	$[0\ \overline{1}\ \overline{1}]$	$(\overline{1}\ 1\ \overline{1})$
2	$[1\ 0\ \overline{1}]$	$(1\ 1\ 1)$	6	$[0\ 1\ \overline{1}]$	$(1\ \overline{1}\ \overline{1})$	10	$[1\ \overline{1}\ 0]$	$(\overline{1}\ \overline{1}\ 1)$
3	$[0\ \overline{1}\ 1]$	$(1\ 1\ 1)$	7	$[1\ 1\ 0]$	$(\overline{1}\ 1\ \overline{1})$	11	$[\overline{1}\ 0\ \overline{1}]$	$(\overline{1}\ \overline{1}\ 1)$
4	$[\overline{1}\ \overline{1}\ 0]$	$(1\ \overline{1}\ \overline{1})$	8	$[\overline{1}\ 0\ 1]$	$(\overline{1}\ 1\ \overline{1})$	12	$[0\ 1\ 1]$	$(\overline{1}\ \overline{1}\ 1)$

⟨tab_fcc⟩

2.6 Irreversibility constraint

The irreversibility of the crack phase-field during loading/unloading, a critical feature of the theory, is ensured by the introduction of the following local history variable

$$\mathcal{H}_e\left(\boldsymbol{x},t\right):=\max_{\tau\in[0,t]}\hat{\psi}^{+}_{e}\left(\boldsymbol{E}^{\mathrm{e}}\left(\boldsymbol{x},\tau\right)\right)\tag{40}$$ eq:He

into eq. (36). The variable $\mathcal{H}_e$ represents the maximum positive elastic energy obtained in a loading process and stems from the work of Miehe et al. (2010) on phase-field modelling of brittle fracture.

2.7 Elastic region, yield function and flow relations

Assuming that the inequality (28) holds (as it does for the choice of g presented in eq. (33)), and hence the reduced dissipation inequality takes the classical form (27) not involving the phase field, then the yield function and flow relations follow as in the "classical" theory of plasticity (see e.g. Simo and Hughes, 1998). The plastic flow relations are now constructed so as to ensure that eq. (27) is satisfied, i.e. to ensure that the plastic dissipation $D^{\mathrm{p}} \geq 0$.

The resolved shear stress τ^α on Γ^α is equivalent to π^α from eq. (7). The yield function for Γ^α is defined by

$$f^\alpha = |\tau^\alpha| - \underbrace{(Y_0 - g^\alpha)}_{Y^\alpha} \leq 0 \tag{41}$$ f_alpha

where Y_0^α and Y^α are the initial and current values of the yield stress on Γ^α. The yield stress evolves from its initial state due to hardening, as captured by the terms g^α.

Assuming rate-independent behaviour and an associative flow rule, the slip rate and the hardening rate, which are conjugate to τ^α and g^α respectively, are given by the normality relations

$$\begin{aligned} \dot\gamma^\alpha &= \lambda^\alpha \frac{\partial f^\alpha}{\partial \tau^\alpha} = \lambda^\alpha \mathrm{sgn}\tau^\alpha \,, \\ \dot\eta^\alpha &= \lambda^\alpha \frac{\partial f^\alpha}{\partial g^\alpha} = \lambda^\alpha = |\dot\gamma^\alpha| = \dot\gamma^\alpha_{\mathrm{acc}} \,, \end{aligned} \tag{42}$$ eq:flow

where $\lambda^\alpha \geq 0$ is a scalar multiplier and $\dot\gamma^\alpha_{\mathrm{acc}}$ is the accumulated slip rate. The normality relations are subject to the Kuhn–Tucker complementarity conditions

$$f^\alpha \leq 0 \qquad \lambda^\alpha \geq 0 \qquad \lambda^\alpha f^\alpha = 0 \,,$$

for each Γ^α.

Under the assumption of plastic flow (i.e. $\dot\gamma^\alpha \neq 0$) the flow relation (42) may be inverted by introducing the dissipation function D defined by

$$D(\dot\gamma^\alpha) = Y^\alpha |\dot\gamma^\alpha| = Y^\alpha \dot\gamma^\alpha_{\mathrm{acc}} \,.$$

This allows the flow relation to be written in the form

$$\begin{aligned} \tau^\alpha &= \frac{\partial D}{\partial \dot\gamma^\alpha} \\ &= Y^\alpha \frac{\dot\gamma^\alpha}{|\dot\gamma^\alpha|} = Y^\alpha \,\mathrm{sgn}\,\dot\gamma^\alpha \end{aligned} \tag{43}$$ flowinv

for $\dot\gamma^\alpha \neq 0$. The flow relation in the equivalent form (43) is an important inverted form, as it allows for the formulation of the incremental problem as a minimization problem. This is in turn advantageous from a computational point of view: see Section 3.

2.8 Viscoplastic regularization

The rate-independent theory presents various numerical challenges due to the indeterminacy of the plastic slip (Schmidt-Baldassari, 2003; Schröder and Miehe, 1997; Miehe and Schröder, 2001). To circumvent these

problems, different rate-dependent regularizations have been proposed (see e.g. Schröder and Miehe, 1997; Miehe and Schröder, 2001, for an overview of various alternatives). In this work, a viscoplastic regularization following Norton, Hoff and Friaâ (Norton, 1929; Hoff, 1954; Friaâ, 1978) of the flow relations is employed. The yield function for each slip system (see eq. (41)) is first recast in the form of a gauge Φ^α defined by

$$\Phi^\alpha := \frac{|\tau^\alpha|}{Y_0 - g^\alpha} \leq 1 \,.$$

The Norton–Hoff viscoplastic regularization amounts to replacing the flow rule (42) by

$$\dot{\gamma}^\alpha = \frac{\partial \bar{f}^\alpha}{\partial \tau^\alpha} \,, \tag{44}$$ eq:flow_NH

where

$$\bar{f}^\alpha = \frac{d_0}{q} \left[\Phi^\alpha\right]^q \,.$$

Here $d_0 > 0$ is the reference slip rate and $q \geq 2$ is the strain-rate-sensitivity exponent. The evolution equation for the hardening variable is given by

$$\dot{\eta}^\alpha = |\dot{\gamma}^\alpha| = \dot{\gamma}^\alpha_{\text{acc}} \,. \tag{45}$$ eq:hard_NH

For this particular choice of the viscoplastic regularization, no elastic domain exists and therefore no Kuhn-Tucker complementarity conditions are needed, as all slip systems are active at all times. This is useful from an algorithmic standpoint, as it avoids the complexity inherent in an active set search algorithm. The rate-independent case is recovered in the limit $q \to \infty$.

2.9 Summary of the governing equations

The system of coupled non-linear governing equations is summarized in Table 2. These equations consider the viscous contribution in the phase-field evolution equation as well as the viscoplastic regularization of the flow rule. The degradation function takes the specific form of eq. (33).

2.10 Boundary conditions

The macroscopic boundary conditions are

$$\boldsymbol{u} = \bar{\boldsymbol{u}} \quad \text{on } \partial B_D \qquad \text{and} \qquad \boldsymbol{t} = \bar{\boldsymbol{t}} \quad \text{on } \partial B_N \tag{46}$$ eq:BCs_u

where $\bar{\boldsymbol{u}}$ and $\bar{\boldsymbol{t}}$ are the prescribed displacements and tractions, and ∂B_D and ∂B_N are complementary portions of the boundary ∂B of the domain B. The boundary conditions for the microscopic force are homogeneous Neumann, i.e.

$$\frac{\partial \widetilde{\psi}}{\partial \nabla s} \cdot \boldsymbol{n} = \boldsymbol{\xi} \cdot \boldsymbol{n} = 0 \quad \text{on } \partial B \,, \tag{47}$$ {?}

which, considering eq. (35), can be rewritten as

$$\nabla s \cdot \boldsymbol{n} = 0 \quad \text{on } \partial B \,. \tag{48}$$ eq:BCs_s

$$\mathrm{div}\boldsymbol{T} + \boldsymbol{b} = \boldsymbol{0}$$

$$\boldsymbol{T} = s^{2e^{\mathrm{p}}/e^{\mathrm{p}}_{\mathrm{crit}}} \frac{\partial \hat{\psi}^{+}_{e}(\boldsymbol{E}^{\mathrm{e}})}{\partial \boldsymbol{E}^{\mathrm{e}}} + \frac{\partial \hat{\psi}^{-}_{e}(\boldsymbol{E}^{\mathrm{e}})}{\partial \boldsymbol{E}^{\mathrm{e}}}$$

$$\tau^{\alpha} = \boldsymbol{s}^{\boldsymbol{\alpha}} \cdot \boldsymbol{T}\boldsymbol{m}^{\boldsymbol{\alpha}}$$

$$g^{\alpha} = -\textstyle\sum_{\beta} H^{\alpha\beta}\eta^{\beta}$$

$$\dot{\gamma}^{\alpha} = \frac{\partial \bar{f}^{\alpha}}{\partial \tau^{\alpha}}\,, \quad \bar{f}^{\alpha} = \frac{d_0}{q}\left[\frac{|\tau^{\alpha}|}{Y_0 - g^{\alpha}}\right]^{q}, \quad \dot{\eta}^{\alpha} = |\dot{\gamma}^{\alpha}|$$

$$\dot{e}^{\mathrm{p}} = \textstyle\sum_{\alpha} |\dot{\gamma}^{\alpha}| \geq 0\,, \quad e^{\mathrm{p}}(t) = \textstyle\sum_{\alpha} \int_0^t |\dot{\gamma}^{\alpha}|\, d\tau\,, \quad p = \frac{e^{\mathrm{p}}}{e^{\mathrm{p}}_{\mathrm{crit}}}$$

$$2l\nabla^2 s + \tfrac{1-s}{2l} = \tfrac{2p}{G_c} s^{2p-1}\mathcal{H}_e + \tfrac{\beta}{G_c}\dot{s}$$

Table 2: Governing equations for the rate-independent case.

erning_relations⟩

These boundary conditions are always adopted in phase-field modeling of fracture as they stem naturally from the weak form of the governing equations. They correspond to enforcing that the regularized crack at the boundary is orthogonal to the boundary itself.

3 The variational problem and its algorithmic implementation

iational_problem⟩

3.1 Time discretization

Rothe's method is employed whereby the nonlinear system of governing equations summarised in Table 2 are discretized in time prior to their spatial discretization using the finite element method. The time interval of interest $0 \leq t \leq T$ is partitioned according to $0 = t_0 < t_1 < ... < t_N = T$ with $\triangle t = t_{n+1} - t_n$. The value of a quantity w at time t_n is denoted as w_n, and an increment in w over the time interval Δt is denoted by $\Delta w = w_{n+1} - w_n$. Rate quantities are approximated using a backward Euler scheme, i.e. $\dot{w} \cong \triangle w/\triangle t$. The time discretized forms of the momentum balance and phase-field evolution equations (5) and (37) written at the current time t_{n+1} read

$$\mathrm{div}\,\boldsymbol{T}_{n+1} + \boldsymbol{b}_{n+1} = \boldsymbol{0}\,, \tag{49}$$ eq:mom_bal_n+1

$$2l\nabla^2 s_{n+1} + \frac{1}{2l}(1 - s_{n+1}) - \frac{2p_{n+1}}{G_c} s_{n+1}^{2p_{n+1}-1}\mathcal{H}_e - \frac{\beta}{G_c \Delta t}(s_{n+1} - s_n) = 0\,, \tag{50}$$ eq:pf_evol_n+1

and are complemented by the boundary conditions (46) and (48), also written for t_{n+1}:

$$\boldsymbol{u}_{n+1} = \bar{\boldsymbol{u}}_{n+1} \quad \text{on } \partial B_D \qquad \text{and} \qquad \boldsymbol{t}_{n+1} = \bar{\boldsymbol{t}}_{n+1} \quad \text{on } \partial B_N\,, \tag{51}$$?eq:BCs_u-1?

$$\nabla s_{n+1} \cdot \boldsymbol{n} = 0 \quad \text{on } \partial B\,. \tag{52}$$?eq:BCs_s-1?

An initial condition for the phase field $s_0(\boldsymbol{x}) := s(\boldsymbol{x}, t=0)$ is also required. Note that the applied traction $\bar{\boldsymbol{t}}_{n+1}$ and the body force $\boldsymbol{b}_{n+1}$ are assumed to be known functions of time. The time discretized flow relations for the plastic variables (44) and (45) read

$$\gamma^\alpha_{n+1} = \gamma^\alpha_n + \Delta t \frac{\partial \overline{f}^\alpha}{\partial \tau^\alpha}\bigg|_{n+1}, \tag{53}$$ eq:gamma

$$\eta^\alpha_{n+1} = \eta^\alpha_n + \Delta t \left|\frac{\partial \overline{f}^\alpha}{\partial \tau^\alpha}\right|_{n+1}. \tag{54}$$ eq:eta

Finally, the time-discrete form of the accumulated plastic deformation, see eq. (12), is given by

$$\Delta e^{\mathrm{p}} = \sum_\alpha |\Delta \gamma^\alpha| \,. \tag{55}$$?eq:e_p-1?

3.2 Weak form

The weak form of the governing equations forms the basis for the subsequent numerical approximation using the finite element method. The spaces of displacements V and phase-field parameters W are defined by

$$V = \left\{ \boldsymbol{u} \;:\; u_i,\, \frac{\partial u_i}{\partial x_j} \in L^2(B),\, \boldsymbol{u} = \boldsymbol{0} \text{ on } \partial B_D \right\},$$
$$W = \left\{ s \;:\; s,\, \frac{\partial s}{\partial x_i} \in L^2(B) \right\}.$$

Testing the time discrete governing equations (49) and (50) with arbitrary admissible fields $\delta \boldsymbol{d} := \{\delta \boldsymbol{u}, \delta s\} \in V \times W$, integrating over the domain B, and applying the Gauss theorem as appropriate yields the following weak statements:

$$\int_B \boldsymbol{T}_{n+1} : \delta \boldsymbol{E}\, dv - \int_{\partial B_N} \bar{\boldsymbol{t}}_{n+1} \cdot \delta \boldsymbol{u}\, da - \int_B \boldsymbol{b}_{n+1} \cdot \delta \boldsymbol{u}\, dv = 0\,, \tag{56}$$ eq:gov_u

$$-\int_B 2l \nabla s_{n+1} \cdot \delta \nabla s\, dv + \int_B \frac{1}{2l}[1 - s_{n+1}]\delta s\, dv - \int_B \frac{2p_{n+1}}{G_c} \mathcal{H}_e s_{n+1}^{2p_{n+1}-1} \delta s\, dv - \int_B \frac{\beta}{G_c \Delta t}[s_{n+1} - s_n]\delta s\, dv = 0\,. \tag{57}$$ eq:gov_s

The *incremental* variational problem can be written as an unconstrained minimization problem; details are provided in the Appendix. The incremental variational formulation is particularly attractive from a computational perspective.

3.3 Spatial discretization

The finite element method is used to approximate the position of the material points $\boldsymbol{x} \in B$ and the primary fields $\boldsymbol{d} := \{\boldsymbol{u}, s\}$, their increments and their variations. The domain B is decomposed into a set of non-overlapping hexahedral elements. The primary variables and the spatial position are all approximated from the values at the nodes of the elements using a standard Lagrangian $Q1$ interpolation in $\mathbb{R}^3$ as follows

$$\boldsymbol{d}_{n+1} \approx \boldsymbol{d}^h_{n+1} = \sum_{A=1}^{n_{\mathrm{dof}}} \boldsymbol{\Phi}_A d_A \qquad \text{and} \qquad \delta \boldsymbol{d}_{n+1} \approx \delta \boldsymbol{d}^h_{n+1} = \sum_{A=1}^{n_{\mathrm{dof}}} \boldsymbol{\Phi}_A \delta d_A \tag{58}$$ {?}

where $n_{\text{dof}} = n^u_{\text{dof}} + n^s_{\text{dof}}$ is the total number of degrees of freedom which is obtained as the sum over the displacement degrees of freedom n^u_{dof} and the degrees of freedom associated with the phase field. The basis functions $\boldsymbol{\Phi}_A = \{\boldsymbol{\Phi}^u_A \, \Phi^s_A\}$ associated with degree of freedom A are $n_{\text{dim}} + 1$ vectors with only one non-zero component corresponding to a component of the displacement or the phase field. The interpolations of the primary fields and their gradients are substituted into eqs. (56)–(57) to obtain the discrete system of governing equations whose entries in the global residual vector $\boldsymbol{R} = \{\boldsymbol{R}^u \, \boldsymbol{R}^s\}$ are given by

$$\boldsymbol{R}^u_{A\,n+1} := \int_B \boldsymbol{E}(\delta\boldsymbol{\Phi}^u_A) : \boldsymbol{T}^h_{n+1}\, dx - \int_{\partial B_N} \delta\boldsymbol{\Phi}^u_A \cdot \delta\boldsymbol{t}_{n+1}\, da - \int_B \delta\boldsymbol{\Phi}^u_A \cdot \boldsymbol{b}_{n+1}\, dx\,, \tag{59}$$

$$\begin{aligned} R^s_{A\,n+1} := &- \int_B \nabla\Phi^s_A \cdot 2l\nabla s^h_{n+1}\, dx \\ &+ \int_B \delta\Phi^s_A \left(\frac{1}{2l}\left(1 - s^h_{n+1}\right) - \frac{2p_{n+1}}{G_c}\mathcal{H}_e \left(s^h_{n+1}\right)^{2p_{n+1}-1} - \frac{\beta}{G_c\Delta t}\left(s^h_{n+1} - s^h_n\right)\right) dx \end{aligned} \tag{60}$$

3.4 Global Newton-Raphson scheme

An iterative Newton–Raphson scheme is used to determine the solution $\boldsymbol{d}_{n+1}$ such that $\boldsymbol{R}_{n+1} \approx \boldsymbol{0}$. Let (i) denote the current global iteration count. The approximate solution at iteration (i) of time-step $n+1$ is denoted $\boldsymbol{d}^{(i)} \equiv \boldsymbol{d}^{(i)}_{n+1}$, and the corresponding residual is denoted as $\boldsymbol{R}^{(i)} \equiv \boldsymbol{R}^{(i)}_{n+1}$. The resulting linearised problem for the incremental change in the solution $\mathtt{d}\boldsymbol{d} := \boldsymbol{d}^{(i+1)} - \boldsymbol{d}^{(i)}$ is given by

$$\begin{aligned} \boldsymbol{R}^{(i+1)} &= \boldsymbol{R}^{(i)} + \left.\frac{\partial \boldsymbol{R}}{\partial \boldsymbol{d}}\right|^{(i)} \mathtt{d}\boldsymbol{d} \equiv \boldsymbol{0}\,, \\ \implies \quad \left.\frac{\partial \boldsymbol{R}}{\partial \boldsymbol{d}}\right|^{(i)} \mathtt{d}\boldsymbol{d} &= -\boldsymbol{R}^{(i)}\,. \end{aligned} \tag{61}$$

NR_outer

The linearised global tangent matrix $\boldsymbol{A}$ is defined by

$$\boldsymbol{A}\Big|^{(i)} := \left.\frac{\partial \boldsymbol{R}}{\partial \boldsymbol{d}}\right|^{(i)}\,.$$

The global system is solved iteratively for $\boldsymbol{d}_{n+1}$. The iterative process is terminated when $|\boldsymbol{R}|$ is less than some small tolerance.

In order to achieve an asymptotically quadratic convergence rate of the iterative procedure, the tangent needs to be algorithmically consistent, see Simo and Hughes (1998). In this work, automatic differentiation is used to compute the tangent contributions at the level of the quadrature points. A detailed presentation of the automatic differentiation tools used can be found in Korelc (2002) and Wriggers (2008).

3.5 Local return map

A classical predictor-corrector type strategy (see e.g. Simo and Hughes, 1998) is employed to compute the increment in the plastic slip and the hardening variables at the level of quadrature point of an element. The fully-discrete form of the residual relation (61) is solved subject to the assumption of frozen plastic flow, i.e. $\Delta\boldsymbol{E}^{\text{p}} \equiv \boldsymbol{0}$. The displacement field $\boldsymbol{u}^{(i)}$ and hence the strain field $\boldsymbol{E}^{(i)}$ is thus known from the current iteration of the global Newton scheme. The split of $\boldsymbol{E}^{(i)}$ into elastic and plastic components is done via a classical, local return map procedure at the quadrature point level (Simo and Hughes, 1998).

The discrete form of the flow relations (53) and (54) yields the following coupled system of non-linear local residual equations:

$$R^\alpha_\gamma = \gamma^\alpha_{n+1} - \gamma^\alpha_n - \Delta t \left.\frac{\partial \overline{f}^\alpha}{\partial \tau^\alpha}\right|_{n+1}, \tag{62}$$

$$R^\alpha_\eta = \eta^\alpha_{n+1} - \eta^\alpha_n - \Delta t \left|\left.\frac{\partial \overline{f}^\alpha}{\partial \tau^\alpha}\right|\right|_{n+1}. \tag{63}$$

A local Newton–Raphson scheme is employed the solve this system approximately. The set of unknown values is defined by $\underline{\Gamma} := \{\underline{\gamma}, \underline{\eta}\}$ and the set of residual equations by $\underline{R} := \{\underline{R}_\gamma, \underline{R}_\eta\}$. Let (j) denote the current iteration of the local Newton–Raphson scheme (the return map). The resulting linearized problem takes the form

$$\begin{aligned}
\underline{R}^{(j+1)} &= \underline{R}^{(j)} + \left.\frac{\partial \underline{R}}{\partial \underline{\Gamma}}\right|_{(j)} \mathsf{d}\underline{\Gamma} \equiv \mathbf{0}\,, \\
\boldsymbol{A}\mathsf{d}\underline{\Gamma} &= -\underline{R}^{(i)}\,, \\
\underline{\Gamma}^{(j+1)} &= \underline{\Gamma}^{(j)} + \mathsf{d}\underline{\Gamma}\,.
\end{aligned}$$

The inner Newton scheme terminates when $|\mathsf{d}\underline{\Gamma}|$ is less than a prescribed tolerance. The initial guess for the inner Newton scheme is that $\underline{\Gamma}^{(j=0)} = \underline{\Gamma}_n$.

4 Numerical examples

In this section, the theory developed in the preceding sections is elucidated via a series of numerical examples.

The free energy ψ in eq. (29) is non-convex in $\boldsymbol{u}$ and s. The majority of the numerical solution strategies in the literature solve the system of governing relations summarised in Table 2 using a staggered scheme to circumvent the iterative convergence issues present in non-convex minimization (see e.g. Miehe et al., 2010). The individual sub-problems that comprise the staggered scheme are convex, however convergence of the combined problem is slow. Recently Gerasimov and De Lorenzis (in press) proposed a robust line-search assisted monolithic approach for phase-field simulation of brittle fracture. Heister et al. (2015) circumvented the issues associated with non-convex minimisation by using an explicit extrapolation for the phase field parameter in the elastic contribution to the free energy (see eq. (30)). A monolithic scheme is also adopted here and the viscous term involving the time-rate of change of the phase-field parameter is used to regularize the problem. Future work will explore alternative schemes to treat the non-convex free energy. The emphasis of the current work is on the novel coupling of the phase field and ductile fracture in single crystals.

The hardening potential (34) is chosen to be quadratic and cross-hardening is neglected (i.e. $\widetilde{\rho} = 0$).

The numerical examples and material properties are based on those presented in Ambati et al. (2015) for ductile damage in polycrystalline materials. The material in the numerical examples is modelled as a FCC crystal with the orientations of the slip systems relative to the unit cell given in Table 1. The material properties are reported in Table 3. The meshes were generated so as to ensure that that the phase field length scale was approximately equal to twice the measure of an element.

Table 3: Constitutive parameters used for the numerical examples, unless stated otherwise.

Bulk modulus	κ	71 660	N/mm^2
Second Lamé parameter	μ	27 260	N/mm^2
Initial yield stress	Y_0	345	N/mm^2
Fracture toughness	G_c	9.31	N/mm
Length scale	l	0.2	mm
Threshold for accumulated plastic deformation	$e^{\mathrm{p}}_{\mathrm{crit}}$	0.1	
Strain rate sensitivity exponent	q	10	
Isotropic hardening modulus	H_0	250	N/mm^2
Reference slip rate	d_0	250	N/mm^2
Euler angles	$\{\vartheta_1, \vartheta_2, \vartheta_3\}$	$\{0, 0, 0\}$	$\circ$

o_material_props⟩

4.1 I-shaped specimen

Consider the I-shaped specimen subject to tensile loading shown in Fig. 2. In addition to the boundary conditions indicated, plane-strain conditions are imposed by preventing displacements in the z-direction. Thus, while the elements and the formulation are three dimensional, the problem is effectively two dimensional. The domain is discretized using 10 184 elements. The upper surface of the specimen is displaced a distance of $\overline{u}_y(t) = \overline{\lambda}(t)10$ mm where $\overline{\lambda}(t) = t$ is the dimensionless applied displacement factor and the displacement is applied over 1 s. The phase field viscosity is initially set to $\beta = 50$ Ns/mm.

The relation between the reaction force on the upper surface f_{react} and the load parameter $\overline{\lambda}$ is shown in Fig. 3 (a). The spatial distribution of the value of the degradation function g (given by eq. (33)) at various stages during the loading is shown in Fig. 3 (b)–(e) (the corresponding stage in the loading history is marked in Fig. 3 (a)). The specimen fails due to a diamond shaped crack (region of material with negligible resistance to tensile loading) in the centre of the specimen.

The distribution of the phase field parameter s, for $s \leq 0.3$ superimposed upon the undeformed domain is shown next to the mesh in Fig. 2. It should be noted that small negative values of the phase field can arise.

The distribution of the value of the degradation function g shown in Fig. 3 (b) coincides with the noticeable onset of plastic flow in the global response in Fig. 3 (a). The spatial distribution of the plastic strain accumulation e^{p} at various stages during the loading is shown in Fig. 4 (a)–(d). The distribution of g shown in Fig. 3 (b), indicates that damage occurs initially both in the centre of the specimen and at the transition between the base and central sections of the specimen. The damage in the centre of the specimen dominates the overall response as the loading continues. Global failure has begun at the load stage indicated in Fig. 3 (d) and correspondingly Fig. 4 (c).

The influence of the phase field viscosity β on the relation between the reaction force on the upper surface f_{react} and the load parameter $\overline{\lambda}$ is shown in Fig. 5. The ability to regularize the problem using the viscosity is clear. For $\beta = 1$ and $\beta = 10$ Ns/mm, it is not possible to track the complete failure history due to loss of iterative convergence.

Additional insight into the various parameters introduced in the preceding sections is provided in Fig. 6 where $\overline{\lambda} = 0.7702$ which is close to the point of complete failure. The irreversibility of the phase field is governed by the maximum positive elastic energy $\mathcal{H}_e$ introduced in eq. (40). The distribution of $\mathcal{H}_e$ is

localized in the vicinity of the crack. The accumulated plastic strain $\mathcal{H}_p := e^{\mathrm{p}}$ is also distributed around the crack but is more diffuse than $\mathcal{H}_e$. The failure mechanism is clear from the distribution of the vertical component of the displacement u_y.

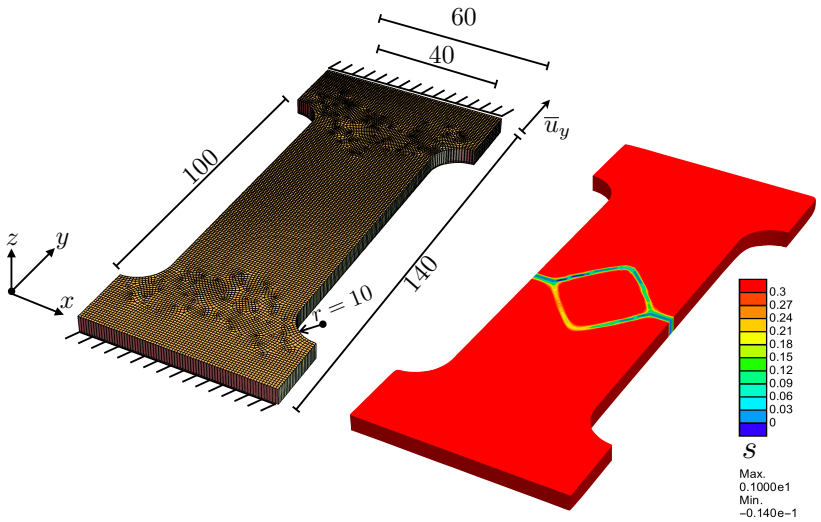

Figure 2: The boundary conditions and loading for the problem of the extension of an I-shaped specimen. Dimensions are in mm. The distribution of the phase-field parameter s at the end of the simulation is also indicated.

I-specimen_setup⟩

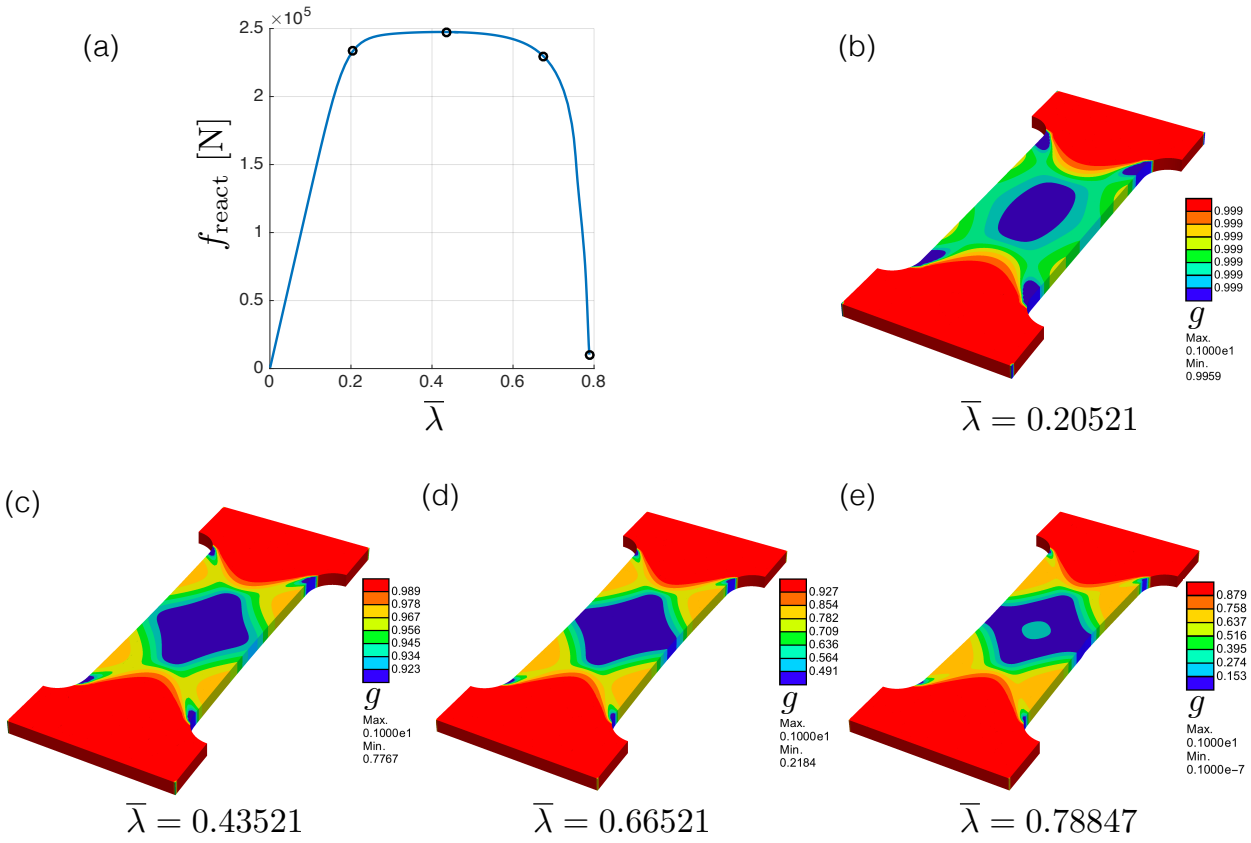

Figure 3: The reaction force on the upper surface of the I-shaped specimen f_{react} versus the load parameter $\overline{\lambda}$ is shown in (a). The distribution of the value of the degradation function g at various points in the load history superimposed upon the deformed specimen is shown in (b)–(e).

pecimen_lambda_f⟩

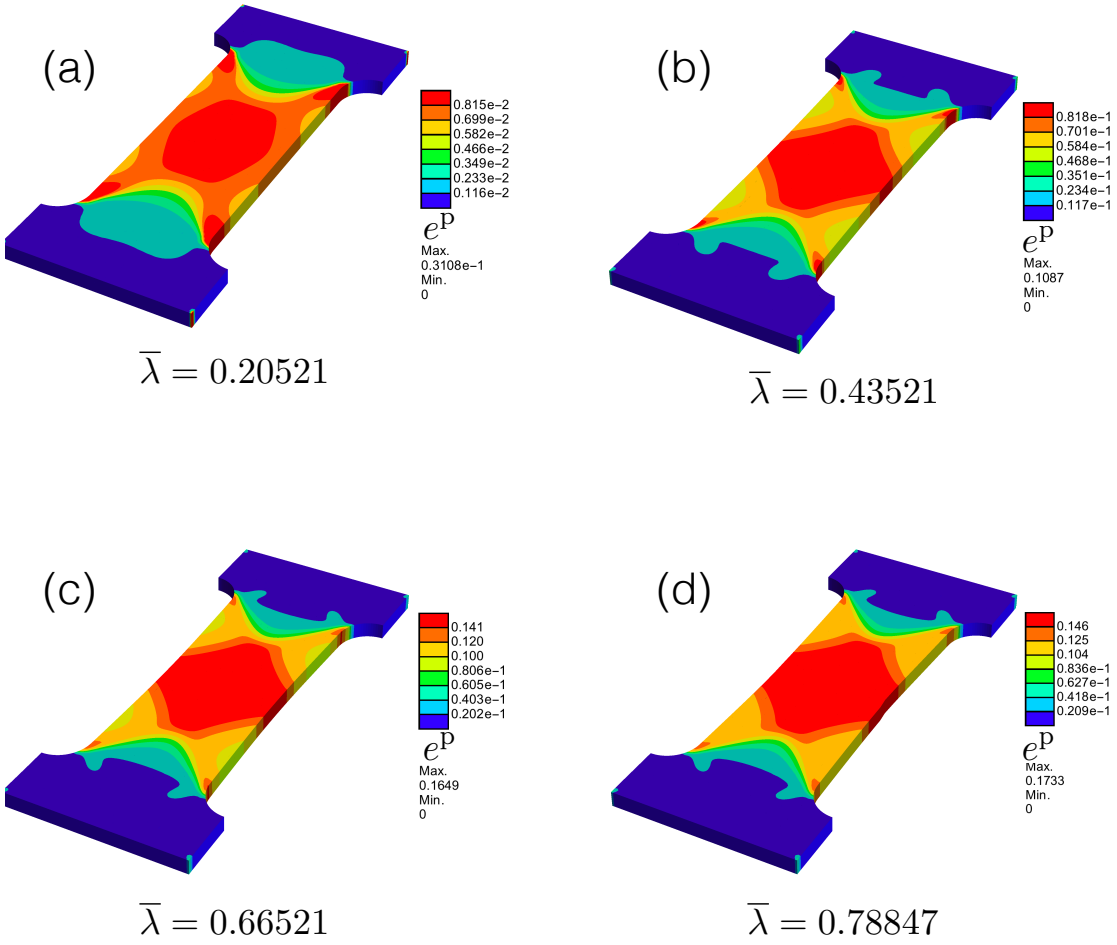

Figure 4: The distribution of the plastic strain accumulation e^{p} at various points in the load history superimposed upon the deformed I-shaped specimen is shown in (a)–(d).

ecimen_lambda_ep⟩

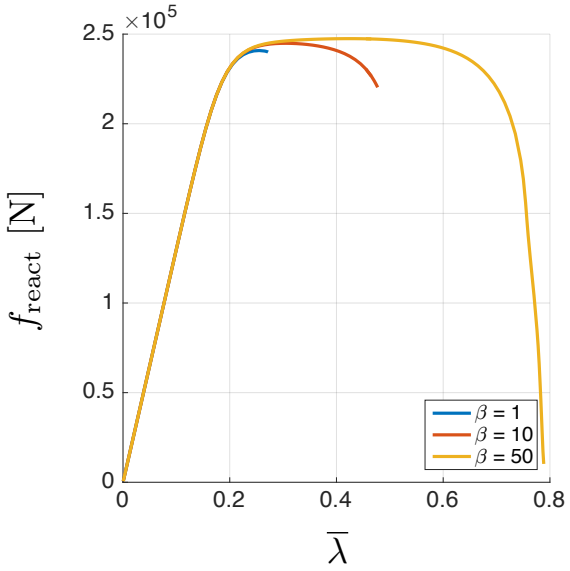

Figure 5: The influence of the phase field viscosity β on the relation between the reaction force on the upper surface of the I-shaped specimen f_{react} and the load parameter $\overline{\lambda}$.

⟨n_lambda_f_betas⟩

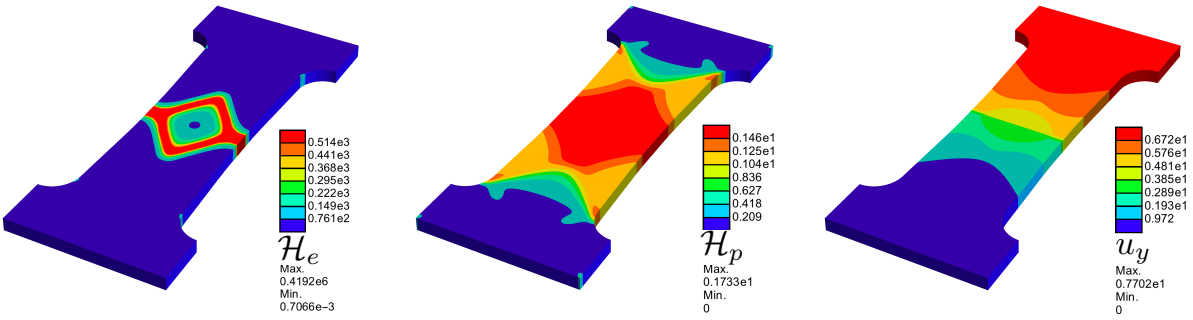

Figure 6: The distribution of the maximum positive elastic energy $\mathcal{H}_e$, the plastic strain accumulation $\mathcal{H}_p$, and the vertical component of the displacement u_y superimposed upon the deformed I-shaped specimen.

⟨I-specimen_H_u⟩

4.2 Asymmetrically notched specimen

Consider the asymmetrically notched specimen subject to tensile loading shown in Fig. 7. In addition to the boundary conditions indicated, plane-strain conditions are imposed by preventing displacements in the z-direction. The upper surface of the specimen is displaced a distance of $\overline{u}_y(t) = \overline{\lambda}(t)1.2$ mm where $\overline{\lambda}(t) = t$ is the applied displacement factor and the displacement is applied over 1 s. The domain is discretized using 20 114 elements.

The influence of the orientation of the crystallographic unit cell is investigated by setting $\vartheta_1 = 0^\circ$ and $\vartheta_1 = 10^\circ$, which corresponds to a rotation around the z-axis. Changing the orientation of the unit cell will alter both the elastic and plastic response. The relation between the reaction force on the upper surface f_{react} and the load parameter $\overline{\lambda}$ for these two choices of Euler angles are shown in Fig. 8. An Euler angle of $\vartheta_1 = 10^\circ$ results in an increased maximum reaction force. The distribution of the phase-field parameter s at the end of the simulation for the two choices of Euler angles is also shown. The failure mode for this example is rapid (i.e. the crack moves rapidly across the specimen) and it is problematic to obtain the converged solution at the point of failure. The phase field is close to zero near the point of crack initiation. Global divergence of the numerical scheme occurs due to an excessively distorted set of elements in this region.

The distribution of the value of the degradation function g, the vertical component of the displacement u_y, the accumulated plastic strain $\mathcal{H}_p := e^{\text{p}}$, and the maximum positive elastic energy $\mathcal{H}_e$ for the two choices of Euler angles are shown in Fig. 9. Both choices result in the failure of the specimen due to a crack extending from one notch to the other. For $\vartheta_1 = 0^\circ$ the damaged region follows a nearly straight path between the notches. For $\vartheta_1 = 10^\circ$ the plastic deformation and damage occurs along a different path. The two cracks extend from the notches. When they reach $y = 25$ they move horizontally and merge. The increased crack length for $\vartheta_1 = 10^\circ$ results in the increase in the maximum reaction force. The maximum positive elastic energy is also greater for $\vartheta_1 = 10^\circ$. The ability of the two distinct damaged regions to merge is a significant advantage of the phase field model over other approaches for modelling fracture and damage that require explicit crack tracking algorithms.

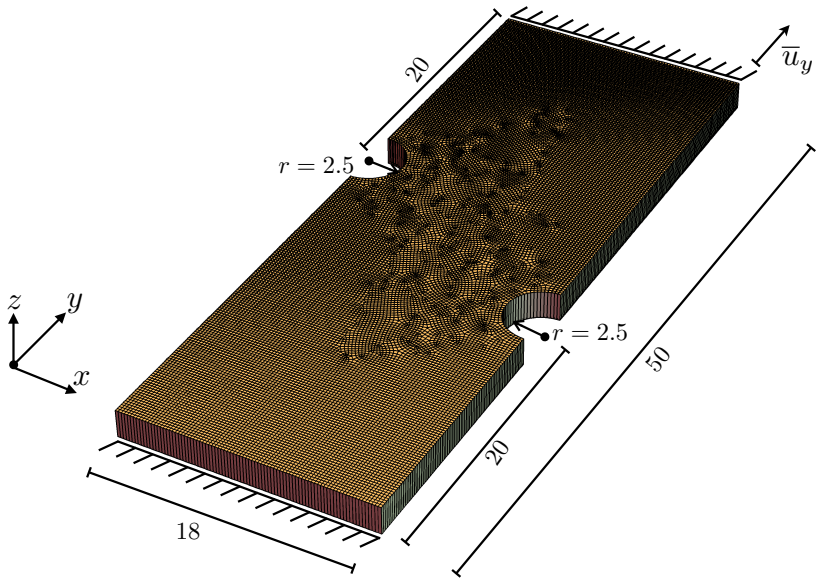

Figure 7: The boundary conditions and loading for the problem of the extension of an asymmetrically notched specimen. Dimensions are in mm.

n_specimen_setup⟩

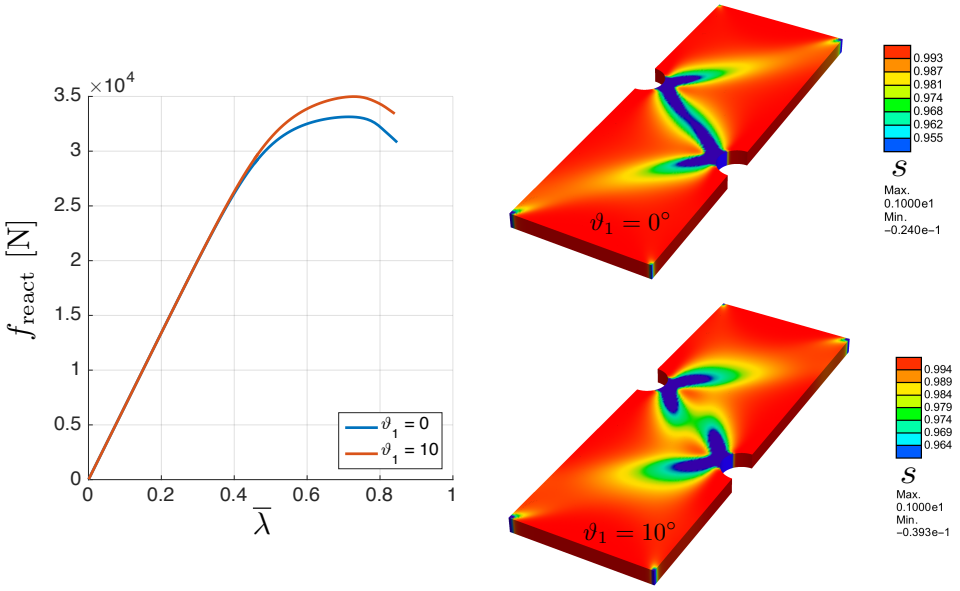

Figure 8: The relation between the reaction force on the upper surface f_{react} and the load parameter $\overline{\lambda}$ for Euler angles of $\vartheta_1 = 0°$ and $\vartheta_1 = 10°$. The distribution of the phase-field parameter s at the end of the simulation is also indicated.

pecimen_lambda_f⟩

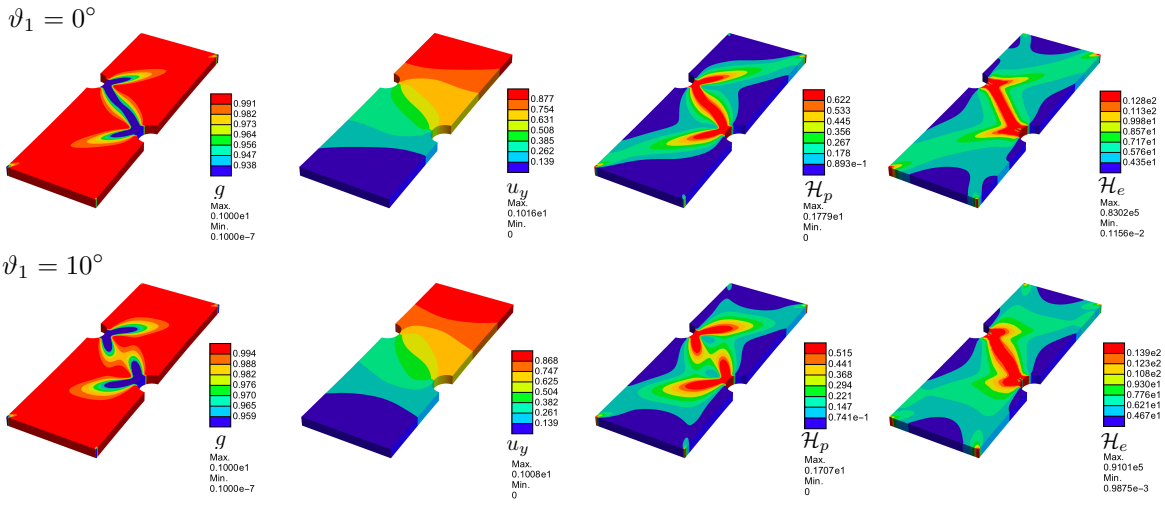

Figure 9: The distribution of the value of the degradation function g, the vertical component of the displacement u_y, the accumulated plastic strain $\mathcal{H}_p := e^{\mathrm{P}}$, and the maximum positive elastic energy $\mathcal{H}_e$ for Euler angles of $\vartheta_1 = 0°$ and $\vartheta_1 = 10°$

n_rotation_plots⟩

5 Conclusions

We proposed a phase-field model for ductile damage and fracture in a single crystal within the kinematically linear regime, by combining the theory of single crystal plasticity as formulated in Gurtin et al. (2010) and the phase-field formulation for ductile fracture proposed by Ambati et al. (2015) within the J_2 plasticity setting. The developed modelling approach introduces coupling between plasticity and fracture through the dependency of the so-called degradation function on a scalar global measure of the accumulated plastic strain on all slip systems. To facilitate the algorithmic implementation and the numerical solution, a viscous regularization is introduced both in the treatment of plasticity, so that all slip systems are active at all times, and in the phase-field evolution equation, which convexifies the originally non-convex minimization problem and thus allows for iterative convergence even within a monolithic solution scheme. Testing of the model on two examples for FCC single crystals indicates that, as in the J_2 plasticity setting, fracture is predicted to initiate and develop in the regions of the maximum accumulated plastic strain, which is in agreement with phenomenological observations. A rotation of the crystallographic unit cell is shown to affect the test results in terms of failure pattern and corresponding global and local response. From the computational standpoint, the viscous regularization of the phase-field governing equation is shown to play an essential role to achieve iterative convergence within a monolithic solution scheme. Future work should include a detailed and comprehensive comparison with test results. From a computational standpoint, iterative convergence of the inviscid formulation solved monolithically can be restored through e.g. the line search procedure developed in Gerasimov and De Lorenzis (in press). Moreover, mesh adaptivity and the adoption of suitable solvers is essential for the efficient and tractable simulation of more realistic problems in three dimensions.

A Incremental variational formulation

We show here that the *incremental* variational problem can be written as an unconstrained minimization problem. For simplicity, we refer to the rate-independent case.

The minimization problem will be one in which the variable e^{p} is kept *fixed*. This may be achieved by setting $e^{\mathrm{p}} = e^{\mathrm{p}}_n$, corresponding to the solution at the previous time-step t_n; or e^{p} may be set equal to a value obtained in the previous iteration during the Newton iterative process. For convenience, we neglect hardening in this treatment: the hardening term is easily included (see the appendix in Reddy (2011)).

The minimization problem reads as follows: find $\boldsymbol{u}_{n+1}$, $\underline{\gamma}_{n+1}$ and s_{n+1} which minimize the functional

$$J\left(\widetilde{\boldsymbol{u}}, \underline{\widetilde{\gamma}}, \widetilde{s}, e^{\mathrm{p}}\right) = \int_B \left[\hat{\psi}_{ec}(\boldsymbol{E}^{\mathrm{e}}(\widetilde{\boldsymbol{u}}, \underline{\widetilde{\gamma}}), \widetilde{s}, e^{\mathrm{p}}) + \sum_\alpha D(\Delta\underline{\widetilde{\gamma}}) + \hat{\psi}_c(\widetilde{s}, \nabla\widetilde{s})\right] dx - \int_B \boldsymbol{b}_{n+1} \cdot \widetilde{\boldsymbol{u}}\, dx - \int_{\partial B_N} \bar{\boldsymbol{t}}_{n+1} \cdot \widetilde{\boldsymbol{u}}\, da$$

over all admissible $\widetilde{\boldsymbol{u}}$, $\underline{\widetilde{\gamma}}$, $\widetilde{s}$, and for fixed e^{p}.

Setting $W = \left(\boldsymbol{u}, \underline{\gamma}, s\right)$, if W is a minimizer of J then

$$J\left(W\right) \leq J\left(\left(1-\theta\right)W + \theta\widetilde{W}\right)$$

for arbitrary but admissible $\widetilde{W}$ and for θ such that $0 < \theta < 1$. Setting

$$\Psi(\widetilde{W}) := \hat{\psi}_{ec}(\boldsymbol{E}^{\mathrm{e}}(\widetilde{\boldsymbol{u}}, \underline{\widetilde{\gamma}}), \widetilde{s}, e^{\mathrm{p}}) + \hat{\psi}_c(\widetilde{s}, \nabla\widetilde{s})$$

we have, from the definition of J and using also the convexity of D,

$$\begin{aligned}\int_B \Big[\Psi(W_{n+1}) + \sum_\alpha D(\Delta\gamma^\alpha)\Big]\,dx \le \int_B \Big[\Psi\big((1-\theta)W_{n+1} + \theta\widetilde{W}\big) + \sum_\alpha D\big((1-\theta)\Delta\gamma^\alpha + \theta\Delta\widetilde{\gamma}^\alpha\big)\Big]\,dx \\ - \theta\Big[\int_B \boldsymbol{b}_{n+1}\cdot(\widetilde{\boldsymbol{u}} - \boldsymbol{u}_{n+1})\;dx + \int_{\partial B_N} \bar{\boldsymbol{t}}_{n+1}\cdot(\widetilde{\boldsymbol{u}} - \boldsymbol{u}_{n+1})\;da\Big] \\ \le \int_B \Big[\Psi\big((1-\theta)W_{n+1} + \theta\widetilde{W}\big) + (1-\theta)\sum_\alpha D(\Delta\gamma^\alpha) + \theta\sum_\alpha D(\Delta\widetilde{\gamma}^\alpha)\Big]\,dx \\ - \theta\Big[\int_B \boldsymbol{b}_{n+1}\cdot(\widetilde{\boldsymbol{u}} - \boldsymbol{u}_{n+1})\;dx + \int_{\partial B_N} \bar{\boldsymbol{t}}_{n+1}\cdot(\widetilde{\boldsymbol{u}} - \boldsymbol{u}_{n+1})\;da\Big]\,.\end{aligned}$$

Rearrangement of the terms and division throughout by θ leads to the inequality

$$\begin{aligned}\int_B \frac{1}{\theta}\Big[\Psi\left((1-\theta)\,W_{n+1} + \theta\widetilde{W}\right) - \Psi\left(W_{n+1}\right)\Big]\;dx + \sum_\alpha \int_B \Big[D(\Delta\widetilde{\gamma}^\alpha) - D(\Delta\gamma^\alpha)\Big]\,dx \\ - \int_B \boldsymbol{b}_{n+1}\cdot(\widetilde{\boldsymbol{u}} - \boldsymbol{u}_{n+1})\,dx - \int_{\partial B_N} \bar{\boldsymbol{t}}_{n+1}\cdot(\widetilde{\boldsymbol{u}} - \boldsymbol{u}_{n+1})\,da \ge 0\,.\end{aligned} \tag{64}$$

eq:A3

By letting θ go to 0 and using the definition of the derivative, (64) becomes

$$\begin{aligned}&\int_B \frac{\partial\Psi}{\partial W}\Big|_{n+1} : (\widetilde{W} - W_{n+1})\,dx + \sum_\alpha \int_B \Big[D(\Delta\widetilde{\gamma}^\alpha) - D(\Delta\gamma^\alpha)\Big]\,dx \\ &- \int_B \boldsymbol{b}_{n+1}\cdot(\widetilde{\boldsymbol{u}} - \boldsymbol{u}_{n+1})\,dx - \int_{\partial B_N} \bar{\boldsymbol{t}}_{n+1}\cdot(\widetilde{\boldsymbol{u}} - \boldsymbol{u}_{n+1})\,da \ge 0\,.\end{aligned} \tag{65}$$

eq:A4

Noting that we can write $\widetilde{W} - W_{n+1} = (\widetilde{W} - W_n) - \Delta W$, if the arbitrary variable $\check{W}$ is defined as $\check{W} = \widetilde{W} - W_n$ then the terms of the form $\widetilde{W} - W_{n+1}$ in eq. (65)) can be replaced by $\check{W} - \Delta W$. With this substitution, eq. (65) becomes

$$\begin{aligned}\int_B \frac{\partial\Psi}{\partial W}\Big|_{n+1} : \big(\check{W} - \Delta W\big)\,dx \;+ \sum_\alpha \int_B \Big[D(\check{\gamma}^\alpha) - D(\Delta\gamma^\alpha)\Big]\,dx \\ - \int_B \boldsymbol{b}_{n+1}\cdot(\check{\boldsymbol{u}} - \Delta\boldsymbol{u})\,dx - \int_{\partial B_N} \bar{\boldsymbol{t}}_{n+1}\cdot(\check{\boldsymbol{u}} - \Delta\boldsymbol{u})\,da \ge 0\,.\end{aligned}$$

Expansion of the integrand in the first term leads to

$$\begin{aligned}&\int_B \Big[\boldsymbol{T}_{n+1} : \Big(\boldsymbol{E}(\check{\boldsymbol{u}}) - \boldsymbol{E}(\Delta\boldsymbol{u}) - \sum_\alpha \boldsymbol{S}^\alpha(\check{\gamma}^\alpha - \Delta\gamma^\alpha\Big) + \frac{\partial\hat{\psi}}{\partial s}\Big|_{n+1}(\check{s} - \Delta s) + \frac{\partial\hat{\psi}}{\partial\nabla s}\Big|_{n+1}\cdot(\nabla\check{s} - \Delta\nabla s)\Big]\,dx \\ &+ \sum_\alpha \int_B \Big[D(\check{\gamma}^\alpha) - D(\Delta\gamma^\alpha)\Big]\,dx - \int_B \boldsymbol{b}_{n+1}\cdot(\check{\boldsymbol{u}} - \Delta\boldsymbol{u})\,dx - \int_{\partial B_N} \bar{\boldsymbol{t}}_{n+1}\cdot(\check{\boldsymbol{u}} - \Delta\boldsymbol{u})\,da \ge 0\,.\end{aligned} \tag{66}$$

eq:A6

If we now set $\check{\gamma}^\alpha = \Delta\gamma^\alpha$ and $\check{s} = \Delta s$, eq. (66)) leads to

$$\int_B \left[\boldsymbol{T}_{n+1} : \left(\boldsymbol{E}^{\mathrm{e}}\left(\check{\boldsymbol{u}}\right) - \boldsymbol{E}^{\mathrm{e}}\left(\Delta\boldsymbol{u}\right)\right)\right] dx - \int_B \boldsymbol{b}_{n+1} \cdot \left(\check{\boldsymbol{u}} - \Delta\boldsymbol{u}\right) dx - \int_{\partial B_N} \bar{\boldsymbol{t}}_{n+1} \cdot \left(\check{\boldsymbol{u}} - \Delta\boldsymbol{u}\right) da \quad \geq \quad 0\,. \qquad (67)$$ eq:A6-1

Setting $\check{\boldsymbol{u}} = \widetilde{\boldsymbol{u}} + \triangle\boldsymbol{u}$ and then $\check{\boldsymbol{u}} = \widetilde{\boldsymbol{u}} - \triangle\boldsymbol{u}$ in (67), we obtain two inequalities of the form $\ldots \geq 0$ and $\ldots \leq 0$, thus giving

$$\int_B \boldsymbol{T}_{n+1} : \boldsymbol{E}\left(\widetilde{\boldsymbol{u}}\right)\, dx - \int_B \boldsymbol{b}_{n+1} \cdot \widetilde{\boldsymbol{u}}\, dx - \int_{\partial B_N} \bar{\boldsymbol{t}}_{n+1} \cdot \widetilde{\boldsymbol{u}}\, da \quad = \quad 0 \qquad (68)$$ eq:A6-1-1

which is the weak form of the momentum balance equation. Next, set in (66) $\check{\boldsymbol{u}} = \triangle\boldsymbol{u}$, $\check{\gamma}^\alpha = \Delta\gamma^\alpha$ for each α. Repeating the procedure used to obtain (68), we get the weak form

$$\int_B \Big[\, \frac{\partial\hat{\psi}}{\partial s}\Big|_{n+1} \widetilde{s} + \frac{\partial\hat{\psi}}{\partial\nabla s}\Big|_{n+1} \cdot \nabla\check{s}\Big] dx \quad = \quad 0$$

of the phase field evolution equation. This leaves the inequality

$$\sum_\alpha \int_B \Big[D(\check{\gamma}^\alpha) - D(\Delta\gamma^\alpha) - \boldsymbol{T}_{n+1} : \sum_\alpha \boldsymbol{S}^\alpha(\check{\gamma}^\alpha - \Delta\gamma^\alpha)\Big]\, dx \geq 0\,.$$

Since $\check{\gamma}^\alpha$ is arbitrary the integrand must satisfy

$$D(\check{\gamma}^\alpha) - D(\Delta\gamma^\alpha) - \boldsymbol{T}_{n+1} : \sum_\alpha \boldsymbol{S}^\alpha(\check{\gamma}^\alpha - \Delta\gamma^\alpha) \geq 0\,.$$

This is the inverted form of the flow relation. In particular, for $\Delta\gamma^\alpha \neq 0$ the dissipation D is differentiable and we obtain (43) in incremental form: that is,

$$\tau^\alpha = \frac{\partial D}{\partial\Delta\gamma^\alpha}\,.$$

References

Alessi2015 [1] R. Alessi, J. J. Marigo, and S. Vidoli. Gradient damage models coupled with plasticity: Variational formulation and main properties. *Mechanics of Materials*, 80:351–367, 2015.

tidelorenzis [2] M. Ambati and L. De Lorenzis. Phase-field modeling of brittle and ductile fracture in shells with isogeometric NURBS-based solid-shell elements. *Computer Methods in Applied Mechanics and Engineering*, in press, 2016.

Ambati2014 [3] M. Ambati, T. Gerasimov, and L. De Lorenzis. A review on phase-field models of brittle fracture and a new fast hybrid formualtion. *Computational Mechanics*, 55:383–405, 2014.

Ambati2015 [4] M. Ambati, T. Gerasimov, and L. De Lorenzis. Phase-field modeling of ductile fracture. *Computational Mechanics*, 55(5):1017–1040, 2015.

Ambatikruse [5] M. Ambati, R. Kruse, and L. De Lorenzis. A phase-field model for ductile fracture at finite strains and its experimental verification. *Computational Mechanics*, 57:149–167, 2016.

Amor2009 [6] H. Amor, J. J. Marigo, and C. Maurini. Regularized formulation of the variational brittle fracture with unilateral contact: Numerical experiments. *Journal of the Mechanics and Physics of Solids*, 57(8):1209–1229, 2009.

Asaro [7] R.J. Asaro and A. Needleman. Texture development and strain hardening in rate dependent polycrystals. *Acta Metallurgica*, 33:923–953, 1985.

Aslan2011 [8] O. Aslan, N. M. Cordero, A. Gaubert, and S. Forest. Micromorphic approach to single crystal plasticity and damage. *International Journal of Engineering Science*, 49:1311–1325, 2011.

Barbe [9] F. Barbe, S. Forest, and G. Cailletaud. Intergranular and intragranular behavior of polycrystalline aggregates. Part 2: results. *International Journal of Plasticity*, 17:537—563, 2001.

Besson [10] J. Besson. Continuum models of ductile fracture: a review. *International Journal of Damage Mechanics*, 19 (1):3–52, 2010.

Borden2012a [11] M. J. Borden. Isogeometric analysis of phase-field models for dynamic brittle and ductile fracture. *Thesis*, 2012. URL `http://repositories.tdl.org/tdl-ir/handle/2152/ETD-UT-2012-08-6113`.

Borden2012 [12] M. J. Borden, C. V. Verhoosel, M. A. Scott, T. J. R. Hughes, and C. M. Landis. A phase-field description of dynamic brittle fracture. *Computer Methods in Applied Mechanics and Engineering*, 217-220:77–95, 2012.

Bourdin2000 [13] B. Bourdin, G. A. Francfort, and J. J. Marigo. Numerical experiments in revisited brittle fracture. *Journal of the Mechanics and Physics of Solids*, 48(4):797–826, 2000.

Cailletaud [14] G. Cailletaud, O. Diard, F. Feyel, and S. Forest. Computational crystal plasticity: from single crystal to homogenized poycrystals. *Technische Mechanik*, 23(2–4):130—145, 2003.

derichs1969 [15] P. H. Dederichs and G. Leibfried. Elastic Green's function for anisotropic cubic crystals. *Physical Review*, 188(3):1175–1183, 1969.

Duda2015 [16] F. P. Duda, A. Ciarbonetti, P. J. Sánchez, and A. E. Huespe. A phase-field/gradient damage model for brittle fracture in elastic–plastic solids. *International Journal of Plasticity*, 65:269–296, 2015.

Dunne2007 [17] F. P. E. Dunne, A. J. Wilkinson, and R. Allen. Experimental and computational studies of low cycle fatigue crack nucleation in a polycrystal. *International Journal of Plasticity*, 23:273–295, 2007.

Ekh2004 [18] M. Ekh, R. Lillbacka, and K. Runesson. A model framework for anisotropic damage coupled to crystal (visco)plasticity. *International Journal of Plasticity*, 20:2143–2159, 2004.

ancfort1998 [19] G. A. Francfort and J.-J. Marigo. Revisiting brittle fracture as an energy minimization problem. *Journal of the Mechanics and Physics of Solids*, 46(8):1319–1342, 1998.

Friaa1978 [20] A. Friaâ. Le Matériau de Norton–Hoff généralisé et ses applications en analyse limite. *C. R. Acad. Sci.*, A286:953–956, 1978.

rasimov2016 [21] T. Gerasimov and L. De Lorenzis. A line search assisted monolithic approach for phase-field computing of brittle fracture. *Computer Methods in Applied Mechanics and Engineering*, in press. ISSN 0045-7825. doi: http://dx.doi.org/10.1016/j.cma.2015.12.017.

tschalk2016 [22] D. Gottschalk, A. McBride, B.D. Reddy, A. Javili, P. Wriggers, and C.B. Hirschberger. Computational and theoretical aspects of a grain-boundary model that accounts for grain misorientation and grain-boundary orientation. *Computational Materials Science*, 111:443 – 459, 2016.

Gurtin2010a [23] M. E Gurtin, E. Fried, and L. Anand. *The Mechanics and Thermodynamics of Continua*. Cambridge University Press, Leiden, 2010.

Heister2015 [24] T. Heister, M. F. Wheeler, and T. Wick. A primal-dual active set method and predictor-corrector mesh adaptivity for computing fracture propagation using a phase-field approach. *Computer Methods in Applied Mechanics and Engineering*, 290:466 – 495, 2015.

Markert [25] C. A. Hernandez Padilla and B. Markert. A coupled ductile fracture phase-field model for crystal plasticity. *Continuum Mechanics and Thermodynamics*, in press, 2015.

Hill [26] R. Hill. Continuum micro-mechanics of elastoplastic polycrystals. *Journal of the Mechanics and Physics of Solids*, 13:89–101, 1965.

Hoff1954 [27] N. J. Hoff. Approximate analysis of structures in the presence of moderately large creep deformations. *Quarterly of Applied Mathematics*, 12(1):49–55, 1954.

Kalidindi [28] S. R. Kalidindi, C. A. Bronkhorst, and L. Anand. Crystallographic texture evolution in bulk deformation processing of fcc metals. *Journal of the Mechanics and Physics of Solids*, 40:536–569, 1992.

Korelc2002 [29] J. Korelc. Multi-language and multi-environment generation of nonlinear finite element codes. *Engineering with Computers*, 18(4):312–327, 2002.

Kuhn2010 [30] C. Kuhn and R. Müller. A continuum phase field model for fracture. *Engineering Fracture Mechanics*, 77 (18):3625–3634, 2010. URL http://dx.doi.org/10.1016/j.engfracmech.2010.08.009.

Mandel [31] J. Mandel. Généralization de la théorie de plasticité de W. T. Koiter. *International Journal of Solids and Structures*, 1:273–295, 1965.

Miehe2001 [32] C. Miehe and J. Schröder. A comparative study of stress update algorithms for rate-independent and rate-dependent crystal plasticity. *International Journal for Numerical Methods in Engineering*, 50:273–298, 2001.

Miehe2010a [33] C. Miehe, M. Hofacker, and F. Welschinger. A phase field model for rate-independent crack propagation: Robust algorithmic implementation based on operator splits. *Computer Methods in Applied Mechanics and Engineering*, 199(45-48):2765–2778, 2010.

MikaDawson [34] D. Mika and P. Dawson. Effects of grain interaction on deformation in polycrystals. *Material Science and Engineering*, A257(62–76), 1998.

Norton [35] F. H. Norton. *Creep of Steel at High Temperatures*. McGraw-Hill, New York, 1929.

Peirce1983 [36] D. Peirce, R.J. Asaro, and A. Needleman. Material rate dependence and localized deformation in crystalline solids. *Acta Metallurgica*, 31(12):1951 – 1976, 1983.

Reddy2011a [37] B. D. Reddy. The role of dissipation and defect energy in variational formulations of problems in strain-gradient plasticity. part 1: polycrystalline plasticity. *Continuum Mechanics and Thermodynamics*, 23(6): 527–549, 2011.

Rice [38] J. Rice. Inelastic constitutive relations for solids: an internal-variable theory and its applications to metal plasticity. *Journal of the Mechanics and Physics of Solids*, 19:443–455, 1971.

Roters [39] F. Roters, P. Eisenlohr, L. Hantcherli, D. D. Tjahjanto, T. R. Bieler, and D. Raabe. Overview of constitutive laws, kinematics, homogenization and multiscale methods in crystal plasticity finite-element modeling: theory, experiments. *Acta Materialia*, 58:1152–1211, 2010.

dassari2003 [40] M. Schmidt-Baldassari. Numerical concepts for rate-independent single crystal plasticity. *Computer Methods in Applied Mechanics and Engineering*, 192:1261–1280, 2003.

chroder1997 [41] J. Schröder and C. Miehe. Aspects of computational rate-independent crystal plasticity. *Computational Materials Science*, 9:168–176, 1997.

Simo1998 [42] J. C. Simo and T. J. R. Hughes. *Computational Inelasticity*, volume 7 of *Interdisciplinary Applied Mathematics*. Springer-Verlag New York, Inc, 1998.

Staroselsky [43] A. Staroselsky and L. Anand. Inelastic deformation of polycrystalline f.c.c. materials by slip and twinning. *Journal of the Mechanics and Physics of Solids*, 46:671—696, 1998.

Taylor [44] G .I. Taylor. Plastic strain in metals. *Journal of the Institute of Metals*, 62:307–324, 1938.

Teodosiu [45] C. Teodosiu and F. Sidoroff. A theory of finite elastoviscoplasticity of single crystals. *International Journal of Engineering Science*, 14:165–176, 1976.

Ulmer2013 [46] H. Ulmer, M. Hofacker, and C. Miehe. Phase Field Modeling of Brittle and Ductile Fracture. *Proceedings in Applied Mathematics and Mechanics*, 13(1):533–536, 2013. URL http://doi.wiley.com/10.1002/pamm.201310258.

Wick [47] D. Wick, T. Wick, R. J. Hellmig, and H. J. Christ. Numerical simulations of crack propagation in screws with phase-field modeling. Technical Report 11, 2015.

riggers2008 [48] P. Wriggers. *Nonlinear finite element methods*. Springer, 2008.